J. Fluid Mech. (2020), *vol.* 894, A17. © The Author(s), 2020.
Published by Cambridge University Press
doi:10.1017/jfm.2020.267

Falling liquid films in narrow tubes: occlusion scenarios

Georg F. Dietze[1,†], G. Lavalle[2,‡] and C. Ruyer-Quil[3]

[1]Université Paris-Saclay, CNRS, FAST, 91405 Orsay, France

[2]Université Paris-Saclay, CNRS, LIMSI, 91405 Orsay, France

[3]Université Savoie Mont Blanc, CNRS, LOCIE, 73376 Le Bourget du Lac, France

(Received 29 October 2019; revised 26 February 2020; accepted 28 March 2020)

We study a gravity-driven wavy liquid film falling down the inner surface of a narrow cylindrical tube in the presence of an active core gas flow. We employ the model of Dietze and Ruyer-Quil (*J. Fluid Mech.*, vol. 762, 2015, pp. 68–109) to investigate the role of surface waves in the occlusion of the tube. We consider four real working liquids and reproduce several experiments from the literature, focusing on conditions where the Bond number is greater or equal to unity. We prove that occlusion is triggered by spatially growing surface waves beyond the limit of saturated travelling-wave solutions, and delimit three possible regimes for a naturally evolving wavy film: (i) certain occlusion, when the liquid Reynolds number is greater than the limit of the spatially most amplified travelling waves. Occlusion is caused by surface waves emerging from linear wave selection (scenario I); (ii) conditional occlusion, when the most amplified waves possess travelling states but longer waves do not. Occlusion is triggered by secondary instability, generating long waves through nonlinear coarsening dynamics (scenario II); and (iii) impossible occlusion, when travelling waves always exist, no matter how great their wavelength. We show that certain occlusion is delayed by gravity and precipitated by a counter-current gas flow, axial viscous diffusion (high-viscosity liquids) and inertia (low-viscosity liquids). The latter two effects are also found to determine whether the occlusion mechanism is dictated by loss of travelling-wave solutions or absolute instability. Finally, we show that occlusion can be prevented through coherent inlet forcing. As a side benefit, we introduce an augmented version of our model based on a localized additional force term that allows representing stable travelling liquid pseudo-plugs.

Key words: thin films, capillary flows

1. Introduction

We consider the configuration in figure 1, a thin liquid film falling down the inner surface of a vertical cylindrical tube of radius $R^\star$ under the action of the gravitational

† Email address for correspondence: dietze@fast.u-psud.fr

‡ Present address: Institut de Mécanique des Fluides de Toulouse (IMFT) - Univ. de Toulouse, CNRS-INPT-UPS, Toulouse, France

https://doi.org/10.1017/jfm.2020.267 Published online by Cambridge University Press

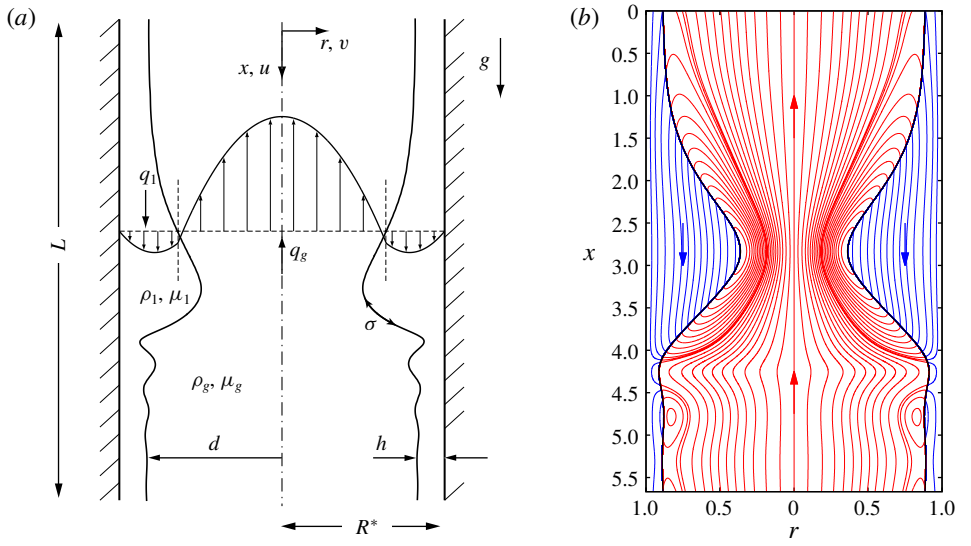


FIGURE 1. Falling liquid film (subscript l) lining the inner surface of a narrow cylindrical tube in contact with a laminar gas flow in the core (subscript g). (*a*) Problem configuration and notations. The tube radius $R^\star$ is the length scale, the star superscript designating dimensional quantities. (*b*) Example of a travelling-wave computation with our model (2.5): case 4 in table 1 (low-viscosity silicone oil), $Re = 14.6$, $Re_g = -17.27$ (limit point marked by an asterisk in figure 13*a*). Streamlines in the wall-fixed reference frame within the liquid (blue lines) and gas (red lines).

acceleration g. The film of liquid (denoted with the subscript l) is in contact with a laminar flow of gas in the core (subscript g). Both fluids are assumed to be Newtonian with constant densities ρ_l and ρ_g, dynamic viscosities μ_l and μ_g, and surface tension σ. Also, we assume the arrangement to be axisymmetric. We denote the film thickness h, the core radius d, its spatial average $\bar{d}$ and the flow rates q_l and q_g. Their dimensional counterparts will be distinguished by a star, e.g. $d^\star$, and their counterparts in the corresponding flat-film primary flow will be denoted with a subscript zero, e.g. d_0.

We focus on conditions, where: (i) the effect of gravity, quantified through the Bond number $Bo = \rho_l g R^{\star 2}/\sigma$, is at least comparable to that of capillarity ($Bo \geqslant 1$); (ii) the liquid film's inertia, quantified through the Reynolds number $Re = q^\star_{l0}\rho_l/(\pi R^\star \mu_l)$, is not necessarily negligible ($Re \leqslant 20$); and (iii) the effect of the gas flow can be relevant, but its Reynolds number $Re_g = q^\star_{g0}\rho_g/(\pi R^\star \mu_g)$ remains moderate ($|Re_g| < 20$).

We investigate this flow with the weighted residual integral boundary layer (WRIBL) model of Dietze & Ruyer-Quil (2015), which was previously applied only to gravity-free films. The model accounts for gravity, inertia, full interfacial curvature, axial viscous diffusion and full inter-phase coupling. Our model computations are confronted with our own direct numerical simulations (DNS) in appendix A and figure 5(*d*).

We focus on the occlusion of the narrow tube due to the interfacial instability of the falling liquid film, as observed experimentally by Dao & Balakotaiah (2000) and Camassa, Ogrosky & Olander (2014). Occlusion is relevant for chemical engineering applications such as tubular falling film micro-reactors (Seebauer *et al.* 2012). It also occurs in the human pulmonary airways due to the collapse of the mucus-serous film

https://doi.org/10.1017/jfm.2020.267 Published online by Cambridge University Press

lining their inner surface (Grotberg 2011). In the lower generations of bronchioles, the effect of gravity and possibly inertia is not necessarily negligible (Kamm & Schroter 1989).

The falling liquid film is subject to two instability mechanisms causing interfacial deformations: the Plateau–Rayleigh mechanism (Plateau 1849; Rayleigh 1892; Goren 1962), due to the azimuthal curvature of the film surface; and the Kapitza mechanism (Kapitza 1948), due to inertia, which sets in as a result of the gravity-driven mean flow (Brooke Benjamin 1957; Yih 1963). The strength of this mean flow determines whether the absolute nature of the Plateau–Rayleigh instability or the convective nature of the Kapitza instability dominates (Duprat *et al.* 2007). For the liquids studied here, we find that occlusion is dictated by absolute instability when $Bo \ll 1$, whereas convective instability is responsible for occlusion when $Bo \geqslant 1$.

In the case of convective instability, the liquid film can produce travelling surface waves, which remain stationary in their reference frame. Gravity plays an important role in shaping these waves, compressing the leading and elongating the trailing wave front, which results in asymmetric tear-shaped wave humps (Dietze 2016). The resulting distortion of the film surface favours variations in axial (stabilizing) over azimuthal (destabilizing) surface curvature. In related systems, this mechanism has been found to saturate the Plateau–Rayleigh instability in the weakly nonlinear regime (Frenkel *et al.* 1987), to the extent that the film looks stable to the naked eye (Quéré 1990). In our current problem, we find that it greatly extends the region of existence of strongly nonlinear travelling waves and considerably delays occlusion.

Trifonov (1992) applied the integral boundary layer approach of Shkadov (1967) to model an annular liquid film falling in a vertical cylindrical tube. The author found that the Plateau–Rayleigh mechanism systematically increases the amplitude of travelling waves versus a planar falling liquid film, where only the Kapitza mechanism is active. He also observed catastrophic growth, when the amplitude of travelling-wave solutions diverged as a function of $1/R$. In those instances, the effect of gravity was negligible, i.e. $Bo \ll 1$. By contrast, we focus on occlusion in the limit $Bo \geqslant 1$. Moreover, the model of Trifonov (1992) did not account for axial viscous diffusion, which we find to greatly precipitate occlusion in high-viscosity films.

Dao & Balakotaiah (2000) performed falling-film experiments in long narrow tubes and determined the occlusion onset in terms of Re for a wide range of liquids. However, no information was available on the wave dynamics responsible for occlusion. By reproducing two of these experiments (runs 13 and 20 there) with our own spatio-temporal computations, we provide this missing information, leading us to distinguish two wave-induced occlusion scenarios. In scenario I, waves causing occlusion emerge directly from linear wave selection. In scenario II, they result from the secondary instability of a regular train of travelling waves, triggering a cascade of coalescence/absorption events that produce increasingly long, more dangerous, waves. The secondary instability (Liu & Gollub 1993) and the ensuing cascaded coarsening dynamics (Chang *et al.* 1996*b*) are well-known phenomena in planar falling liquid films.

Jensen (2000) investigated annular collars travelling on a gravity-driven liquid film lining the inner surface of a cylindrical tube. The collars were constructed from unduloids, i.e. symmetric constant-curvature equilibrium shapes (Delaunay 1841). The author studied under what conditions collars may grow to occlude the tube. Our study extends this work in that the collar shape is not forced to be symmetric, but follows implicitly from the evolution equations. This allows for the gravity-induced distortion of collars, which we find can greatly delay occlusion.

https://doi.org/10.1017/jfm.2020.267 Published online by Cambridge University Press

Camassa *et al.* (2014) performed falling-film occlusion experiments in a transparent tube, using a high-viscosity silicone oil. By confronting these with linear stability calculations, the authors concluded that occlusion is caused by spatially growing nonlinear waves and not by absolute linear instability ($Bo = 11.06$ in their experiments). Furthermore, with the help of a first-order long-wave model obtained from asymptotic expansion (Benney 1966), the authors constructed travelling-wave solutions. By continuing these at fixed wavelength in terms of Re, they identified a limit point, and conjectured that this may signal the occlusion onset in a real system. However, the authors cautioned that further work was needed to verify this with respect to their experiments. This work was initiated by Camassa *et al.* (2016), but their model did not account for axial viscous diffusion, which we show to strongly affect travelling-wave solutions, and the wavelength assumed in their continuation was too long compared to the experiment.

In our current study, we have checked the conjecture of Camassa *et al.* (2014) based on travelling-wave and spatio-temporal computations with our model. We have successfully confronted these computations with the experiments of Camassa *et al.* (2014) and find that accounting for axial viscous diffusion greatly improves agreement. Based on our computations, we find that the surface waves causing occlusion indeed systematically lie beyond the limit of travelling-wave solutions (figure 4), confirming the conjecture of Camassa *et al.* (2014). This limit is highly sensitive to the considered wavelength, long waves being more dangerous than short waves, as shown by Camassa *et al.* (2016) and Ding *et al.* (2019). Thus, any predictive criterion for occlusion based on travelling-wave solutions must account for the type of waves that actually occur in a real system.

For this, we introduce the upper conservative occlusion bound Re_{max}, which corresponds to the limit point of travelling-wave solutions at the spatially most amplified frequency of linear waves f_{max}. For $Re > Re_{max}$, the most amplified surface waves, which typically emerge in an experiment, do not possess travelling states and occlusion is certain to occur in a naturally evolving film. We find that the occlusion experiments of Camassa *et al.* (2014) and experimental run 20 in Dao & Balakotaiah (2000) correspond to this regime. Occlusion in this case occurs through scenario I. To determine Re_{max} we have computed the most amplified wave frequency f_{max} in our numerical continuations by solving the linear spatial stability problem along with our nonlinear model equations. This had not been attempted by Camassa *et al.* (2014) and Ding *et al.* (2019).

At the other end, occlusion is delimited by a lower conservative bound $Re = Re_0$, below which travelling-wave solutions always exist, no matter how great the wavelength, and occlusion is impossible. The existence of such a limit was discovered by Ding *et al.* (2019).

We find that the conservative occlusion bounds Re_0 and Re_{max} delimit a region of conditional occlusion, $Re_0 < Re < Re_{max}$, where occlusion is theoretically possible (for long enough waves) but does not necessarily occur in a real system. Whether it does, depends on the specific wave dynamics that unfold over the spatio-temporal evolution of the film, and whether the tube is long enough to accommodate this. In this regime, we find that occlusion is caused by scenario II and that it applies to experimental run 13 in Dao & Balakotaiah (2000). It also opens the possibility of preventing occlusion through coherent inlet forcing, i.e. by forcing waves of sufficiently high frequency. We validate this idea based on spatio-temporal computations.

Unless Bo is very large, we find that the height of the travelling waves at the limit point $Re = Re_{max}$ is far from reaching the tube radius. In contrast to what Dao &

https://doi.org/10.1017/jfm.2020.267 Published online by Cambridge University Press

Balakotaiah (2000) conjectured, travelling-wave solutions are thus lost abruptly and not due to the wave height reaching the tube radius continuously.

Zhou *et al.* (2016) investigated viscoelastic liquid films falling in a deformable narrow tube. The authors performed calculations with a model based on the same approach as Trifonov (1992), which does not account for axial viscous diffusion. Interestingly, it was shown that occlusion can cause a contraction of the flexible tube. Such events are known to occur in the pulmonary airways (Grotberg 2011) and can damage cells within the capillaries (Bian *et al.* 2010). The authors went on to determine the occlusion onset by varying the liquid flow rate in spatio-temporal computations. This onset was defined as the point at which the computation breaks down due to an occlusion event. However, such computations cannot attain a representative developed state. For example, when starting from a flat-film initial condition, a single unrealistically large tsunami-like wave usually develops in the early stages. This wave is bound to cause occlusion, but it is not representative of a real system. By contrast, we characterize occlusion based on the bounds Re_0 and Re_{max} of travelling-wave solutions, and our spatio-temporal computations have all been continued until reaching a statistically developed state. To achieve this, we have allowed our computations to continue past occlusion events by numerically limiting the core radius of an occluded region to a small but finite value.

Liu & Ding (2017) studied a vertically falling glycerol film flowing down a porous cylindrical surface using a lubrication equation. The authors found that porosity precipitates both the absolute instability threshold and the occlusion limit. Using the same approach, Ding *et al.* (2019) studied the effect of the Marangoni instability on a radially heated liquid film falling in a vertical cylindrical tube. The authors found that Marangoni stresses promote/delay occlusion when the film is heated/cooled from the wall. However, their modelling approach does not account for inertia nor axial viscous diffusion. We find that this does not allow us to accurately predict occlusion in high-viscosity (because of axial viscous diffusion) or low-viscosity (because of inertia) liquids.

The model employed in our current study extends upon the earlier works of Trifonov (1992), Camassa *et al.* (2014), Camassa, Ogrosky & Olander (2017), Zhou *et al.* (2016), Liu & Ding (2017) and Ding *et al.* (2019) by accounting for axial viscous diffusion and inertia. This has allowed us to investigate four real liquids, for which we determine the lower and upper occlusion bounds Re_0 and Re_{max} and characterize the possible occlusion scenarios. When the viscosity is high, we find that axial viscous diffusion greatly precipitates the upper occlusion bound Re_{max} (by 74 % for the high-viscosity silicone oil). When the viscosity is low (low-viscosity silicone oil), inertia cannot be neglected and is found to precipitate Re_{max} by 20 %. We also find that these two effects determine whether the occlusion mechanism is dictated by absolute linear instability or the loss of travelling-wave solutions.

Our model also accounts for full inter-phase coupling between the liquid and gas, and this has allowed us to study the effect of a laminar counter-current gas flow on the occlusion bound Re_{max}. For low-viscosity liquids, where the wave-induced pressure variation in the gas becomes relevant in the liquid force balance, we find that Re_{max} is significantly reduced with increasing $|Re_g|$ (by up to 25 % in our computations). Thereby, the conditions we have studied differ from previous works. Alekseenko *et al.* (2009) experimentally studied the linear stability of a falling liquid film subject to a co-current turbulent gas flow. Their tube radius was large and thus occlusion could not occur. Camassa *et al.* (2012, 2017) studied co-current upward liquid/gas flows based on a long-wave model, where the effect of the (turbulent) gas flow was accounted for

https://doi.org/10.1017/jfm.2020.267 Published online by Cambridge University Press

by relaxing the inter-phase coupling conditions in the limit of high gas velocities. By contrast, we focus on laminar (counter-current) gas flows, where our model, which relies on the unrelaxed coupling conditions, behaves well.

For the case of a planar falling liquid film sheared by a confined gas flow, many works have investigated the flooding phenomenon, where the liquid film either occludes the channel (Vlachos *et al.* 2001), surface waves (Tseluiko & Kalliadasis 2011) or the liquid flow (Trifonov 2010) reverse direction, or the liquid film disintegrates into drops (Zapke & Kröger 2000).

Finally, several works are related less directly to the studied problem. Kouris & Tsamopoulos (2001) studied liquid/liquid gravity-driven flows through a vertical pipe. Beltrame (2018) studied the transition between partial and complete wetting in a microtube. Xu & Jensen (2017) studied migration of liquid films in tubes with rough walls. Moreover, many works have dealt with pressure-driven core-annular flows (Aul & Olbricht 1990; Joseph, Chen & Renardy 1997) or liquid films falling down fibres (Kalliadasis & Chang 1994; Quéré 1999). In the latter case, occlusion cannot occur, unless the gas phase is confined by an additional concentric hollow cylinder (Wray 2013).

Our manuscript is structured as follows. In section 2 we introduce the governing equations, and details of our model (§ 2.1), direct numerical simulations (§ 2.2) and linear stability calculations (§ 2.3). Results are presented in § 3, where we start by proving that occlusion in real systems results from surface waves that lie beyond the limit of travelling-wave solutions (§ 3.1). In § 3.2 we compute the upper and lower occlusion bounds Re_{max} and Re_0, delimiting the regimes of certain, conditional, and impossible occlusion. For one of the studied cases, we validate these results based on our own DNS of travelling-wave solutions. In §§ 3.3 to 3.6 we show how Re_{max} is affected by gravity, axial viscous diffusion, inertia and the core gas flow. In § 3.7 we demonstrate occlusion scenarios I (certain occlusion regime) and II (conditional occlusion regime) by reproducing two of the experimental runs from Dao & Balakotaiah (2000) with spatio-temporal computations. In § 3.8 we show that occlusion in the conditional regime can be prevented through coherent inlet forcing. Conclusions are drawn in § 4. The appendix reports comparisons with transient DNS (appendix A), numerical details regarding our travelling-wave DNS (appendix B), as well as additional discussions of figures 13(*a*) (appendix C) and 4(*a*) (appendix D). Finally, in appendix E we introduce an augmented version of our WRIBL model that allows a better representation of liquid plugs, based on a localized force term.

2. Mathematical description

We consider the flow in figure 1(*a*), which is rotationally symmetric with respect to the tube axis, and is governed by the Navier–Stokes and continuity equations for the liquid (subscript $k = l$, $\chi_l = 1$) and gas (subscript $k = g$, $\chi_g = \Pi_\mu/\Pi_\rho$):

$$\left.\begin{aligned} \mathrm{d}_t u_k &= -\partial_x p_k + Fr^{-2} + \chi_k Re^{-1}\{r^{-1}\partial_r(r\,\partial_r u) + \partial_{xx}u\},\\ \mathrm{d}_t v_k &= -\partial_r p_k + \chi_k Re^{-1}\{\partial_r[r^{-1}\partial_r(rv)] + \partial_{xx}v\},\end{aligned}\right\} \tag{2.1a}$$

$$\partial_x u_k + r^{-1}\partial_r(v_k r) = 0. \tag{2.1b}$$

Here $Re = \rho_l \mathcal{U}\mathcal{L}/\mu_l = q^\star_{l0}/(\pi R^\star)/(\mu_l/\rho_l)$ is the Reynolds number and $Fr = \mathcal{U}/\sqrt{g\mathcal{L}}$ is the Froude number, all variables having been rendered dimensionless with the following reference scales: the length scale $\mathcal{L} = R^\star$, which corresponds to the tube radius, the velocity scale $\mathcal{U} = q^\star_{l0}/\pi/R^{\star 2}$, which corresponds to the surface velocity

https://doi.org/10.1017/jfm.2020.267 Published online by Cambridge University Press

of the liquid, the time scale $\mathcal{T} = \mathcal{L}/\mathcal{U}$ and the pressure scale $\mathcal{P}_k = \rho_k \mathcal{U}^2$, which corresponds to the phase-specific dynamical pressure. The star symbol denotes dimensional quantities, and the subscript zero denotes the flat-film primary flow. Thus, q_{l0} designates the nominal liquid flow rate.

The set of governing equations is completed by the boundary conditions

$$u_l|_{r=R} = v_l|_{r=R} = 0, \quad \partial_r u_g|_{r=0} = v_g|_{r=0} = 0, \tag{2.2a,b}$$

and the kinematic/dynamic inter-phase coupling conditions at the film surface $r = d$:

$$u_l = u_g, \quad v_l = v_g = \partial_t d + u_k \partial_x d, \tag{2.3a}$$

$$\left.\begin{aligned} \tau_l^t &= \Pi_\mu \tau_g^t, \\ \tau_k^t &= \partial_r u_k + \partial_x v_k - 2\partial_x d(1+\partial_x d^2)^{-1}[\partial_x u_k - \partial_r v_k], \end{aligned}\right\} \tag{2.3b}$$

$$\left.\begin{aligned} \tau_l^n + Re\, p_l &= \Pi_\mu \tau_g^n + \Pi_\rho Re\, p_g + ReWe^{-1}\kappa, \\ \tau_k^n &= 2(1+\partial_x d^2)^{-1}[\partial_x d \partial_r u_k - \partial_r v_k - \partial_x d^2 \partial_x u_k + \partial_x d \partial_x v_k]. \end{aligned}\right\} \tag{2.3c}$$

Here τ^t and τ^n designate the tangential and normal interfacial viscous stresses, $\Pi_\rho = \rho_g/\rho_l$ and $\Pi_\mu = \mu_g/\mu_l$ are the density and dynamic viscosity ratios, $We = \rho_l \mathcal{U}^2 \mathcal{L}/\sigma$ is the Weber number and κ denotes the total curvature of the film surface:

$$\kappa = \partial_{xx} d - \frac{1}{d}\left[1 - \frac{1}{2}(\partial_x d)^2\right]. \tag{2.4}$$

We will refer to computations based on the full equations (2.1) to (2.3) as direct numerical simulations. These have been performed for validation purposes and results are reported in appendix A and figure 5(*d*). However, most of our computations were carried out with the WRIBL model of Dietze & Ruyer-Quil (2015), which we introduce next.

2.1. *Weighted residual integral boundary layer model*

The WRIBL model consists of three coupled partial differential equations for the core radius d and the flow rates q_l and q_g (Dietze & Ruyer-Quil 2015):

$$\partial_x q_j - \varepsilon_j 2\pi d \partial_t d = 0, \tag{2.5a}$$

$$\begin{aligned} \{S_i \partial_t q_i + F_{ij} q_i \partial_x q_j + G_{ij} q_i q_j \partial_x d\} &= Fr^{-2}(1-\Pi_\rho) \\ &- We^{-1}\partial_x[\kappa] + Re^{-1}(C_{jl} - \Pi_\mu C_{jg}) q_j \\ &+ Re^{-1}\{J_j q_j (\partial_x d)^2 + K_j \partial_x q_j \partial_x d + L_j q_j \partial_{xx} d + M_j \partial_{xx} q_j\}. \end{aligned} \tag{2.5b}$$

Here the subscripts i and j are to be permuted over the phase indicators for the liquid ($i, j = l$) and gas ($i, j = g$). This yields two equations from (2.5*a*), ensuring integral mass conservation, and one equation from (2.5*b*), which ensures conservation of momentum. The terms on the right-hand side of (2.5*b*) account for different driving forces, i.e. gravity, capillarity and viscous drag. Relating these terms directly to one another yields two alternative dimensionless groups that are also useful for characterizing the studied flow regimes: the Bond number $Bo = We\, Fr^{-2} = \rho_l g R^{\star 2}/\sigma$, which relates gravity to capillarity, and the capillary number $Ca = We/Re = \mu_l \mathcal{U}/\sigma$, which relates viscous drag to capillarity. Following Dao & Balakotaiah (2000), we will also make use of the Kapitza number $Ka = \sigma \rho_l^{-1} g^{-1/3} \mu_l^{-4/3}$ and the Laplace

https://doi.org/10.1017/jfm.2020.267 Published online by Cambridge University Press

number $La = \sigma\rho_l R^\star/\mu_l^2$. We point out however that the list *Re*, *Fr*, *We*, *Bo*, *Ca*, *Ka* and *La* contains only three independent dimensionless groups, e.g. *Re*, *Ka* and *Bo*, which (along with Π_μ and Π_ρ) suffice to fully describe the flow. All other groups can be expressed in terms of these three, e.g. $Ca = Re(BoKa^3)^{-1/2}$.

The model is completed by an equation for the gas pressure gradient $\partial_x p_g|_{r=d}$:

$$\begin{aligned} 2\Pi_\rho Re\partial_x p_g|_{r=d} \;=\; & -Re\{\underline{S}_i\partial_t q_i + \underline{F}_{ij}q_i\partial_x q_j + \underline{G}_{ij}q_i q_j\partial_x d\} \\ & + Re\, Fr^{-2}(1+\Pi_\rho) - We^{-1}\, Re\,\partial_x[\kappa] + (C_{jl} + \Pi_\mu C_{jg})q_j \\ & + \underline{J}_j q_j(\partial_x d)^2 + \underline{K}_j\partial_x q_j\partial_x d + \underline{L}_j q_j\partial_{xx}d + \underline{M}_j\partial_{xx}q_j, \end{aligned} \tag{2.5c}$$

which is used either to evaluate the pressure distribution *a posteriori* or to impose a gas pressure drop through an integral condition. The coefficients F_{ij}, G_{ij}, C_{ij}, S_j, J_j, K_j and M_j in (2.5*b*) and their counterparts marked by an underscore in (2.5*c*) are known functions of d. They can be found in appendix A of Dietze & Ruyer-Quil (2015).

We solve the equation system (2.5) numerically using three approaches: (i) transient periodic computations, where the domain length L corresponds to the wavelength Λ and where $\partial_x^i q_k|_{x=0} = \partial_x^i q_k|_{x=\Lambda}$ and $\partial_x^i d|_{x=0} = \partial_x^i d|_{x=\Lambda}$ for $i = 0, 1, 2, 3$. The code employed for this is based on a Crank–Nicolson time discretization and first-order central differences for spatial discretization (Dietze & Ruyer-Quil 2015); (ii) continuation of periodic travelling-wave solutions that are stationary in the wave-fixed coordinate $\xi = x - ct$ moving with the wave celerity c. These computations were performed with the continuation software AUTO07P (Doedel 2008); (iii) transient open-domain computations with inlet and outlet conditions. At the liquid inlet, $x = 0$, we fix the core radius $d = d_0$ of the flat-film primary flow. For the liquid flow rate q_l, we superimpose a zero-mean temporal perturbation on the nominal value q_{l0}, i.e.

$$q_l(x=0,\, t) = q_{l0}[1 + F(t)], \tag{2.6a}$$

where the function $F(t)$ defines the type of inlet perturbation:

$$F(t) = \epsilon_1 \sin(2\pi f t) + \epsilon_2 \sum_{k=1}^{N} \sin(2\pi k\Delta f t + \varphi_{rand}), \qquad \Delta f = 2f_c/N. \tag{2.6b}$$

The first term in (2.6*b*) constitutes a harmonic perturbation of frequency f and the second term mimics white noise through a series of $N = 1000$ Fourier modes that are shifted by a random phase shift $\varphi_{rand} = \varphi_{rand}(k) \in [0, 2\pi]$ and that span a frequency range of twice the linear cut-off frequency f_c (Chang, Demekhin & Kalaidin 1996*a*). All our computations were run with the same $\varphi_{rand}(k)$ number series, which was generated once and for all with the pseudo random number generator RandomReal in Mathematica (2014). The strength of the two terms in (2.6*b*) is determined through their amplitudes ϵ_1 and ϵ_2. When $\epsilon_1 = 0$, the inlet perturbation consists only of white noise. This setting will be used to simulate the natural, noise-driven, evolution of a wavy film as it would occur in an experiment (§§ 3.1 and 3.7). In § 3.8 we will use coherent inlet forcing to prevent occlusion. In those computations, we will set $\epsilon_1 > 0$, thus adding a monochromatic harmonic perturbation to the inlet noise.

At the outlet, $x = L$, we have implemented the boundary conditions of Richard, Ruyer-Quil & Vila (2016), which ensure that liquid is always sufficiently drained from the domain. We set $d|_{N+2} = d|_{N+1} = d|_N$ and $q_l|_{N+1} = q_{l0}(R - d|_N)^{3/2}/(R - d_0)^{3/2}$, where N corresponds to the last grid point within the domain and $N + 1$, $N + 2$ to the

https://doi.org/10.1017/jfm.2020.267 Published online by Cambridge University Press

two downstream ghost points. Computations were started from the initial condition $d(x, t = 0) = d_0$, $q_l(x, t = 0) = q_{l0}$.

In our codes, the gas flow rate q_g is expressed in terms of the total flow rate q_{tot}, i.e.

$$q_{tot}(t) = q_l(x, t) + q_g(x, t), \tag{2.7}$$

which is spatially invariant. In our computations, we either fix q_{tot} explicitly, which fixes the nominal gas flow rate q_{g0}, given a nominal liquid flow rate q_{l0}. Or q_{tot} is dynamically adjusted to produce a fixed gas pressure drop Δp_g, imposed through an integral condition on (2.5*c*). We quantify this pressure drop through the normalized pressure gradient

$$\Psi = \Delta p_g / LFr^2, \tag{2.8}$$

where L is the domain length. When $\Psi = 1$, the pressure drop exactly balances the weight of the gas column, and we refer to this as the aerostatic situation. This is most realistic for reproducing experiments where the core gas flow is quiescent.

In our transient computations, the wavy liquid film can tend towards occluding the tube. In an experiment such an event would form a liquid plug separated by two gas bubbles. The topological change occurring in this situation cannot be mathematically represented by our model, which implies continuous fluid layers. Thus, we apply a numerical procedure to allow our computations to continue beyond such events. For this, we level the core radius d to an arbitrary value $d_{crit} = 0.1$ whenever/wherever $d \leqslant d_{crit}$. As a result, occluded zones are represented by a thin gas filament connecting two bubbles either side of a liquid plug (figure 3*c*). Although our approach allows us to recover some basic features of these zones, it is a crude and invasive approximation of the actual physics. For example, every time d is reset to d_{crit}, a bit of liquid mass is lost and this can cause the unphysical reopening of liquid plugs (supplementary movies M2 and M3, available at https://doi.org/10.1017/jfm.2020.267). We stress, however, that we are not interested in studying the actual behaviour of occluded zones here. Our current paper focuses on the events leading up to occlusion, and, thus, our numerical limitation of the core radius d is simply a means to continue our computations until a developed state has been reached. Nonetheless, we propose in appendix E an alternative way of representing liquid plugs in the framework of our WRIBL model, based on an additional repulsive force in the momentum equation (2.5*b*) that stabilizes the film surface at very small d. This approach is inspired by the representation of contact line problems with film models (Thiele *et al.* 2001), and confronting it with full-fledged plug models (Suresh & Grotberg 2005; Ubal *et al.* 2008) is an enticing prospect for future work.

2.2. *Direct numerical simulation*

We have validated our model computations with selected DNS based on the full governing equations (2.1)–(2.4). These were performed with two different codes.

Transient simulations were performed with the finite volume solver Gerris (Popinet 2009), which uses the volume of a fluid (Hirt & Nichols 1981) and continuum surface force (Brackbill, Kothe & Zemach 1992) methods to represent the two-phase nature of the flow. We have successfully applied this code to falling liquid films in previous works (Dietze & Ruyer-Quil 2013, 2015; Dietze 2019), where further details are given. In the current work, we have used it to perform axisymmetric transient DNS on a domain spanning the wavelength Λ in streamwise direction and the tube radius R in radial direction, applying periodic streamwise boundary conditions. To allow imposing

https://doi.org/10.1017/jfm.2020.267 Published online by Cambridge University Press

the gas pressure drop Δp_g (2.8) in this periodic setting, the streamwise momentum equations (2.1) for the liquid ($k = l$) and gas ($k = g$) were rewritten in terms of the modified pressure $\tilde{p}_k = p_k + x\Delta p_k/\Lambda$, yielding the additional source term Γ_k:

$$\Gamma_k = \frac{\Delta p_k}{\Lambda}, \quad \Delta p_l = \Pi_\rho \Delta p_g. \tag{2.9a,b}$$

Thanks to this source term, the governing equations can be solved with a periodicity condition on $\tilde{p}_k$, while the actual pressure p_k is subject to a pressure drop, allowing us to control the gas flow rate. Our transient DNS were started from a flat-film initial condition corresponding to the primary flow. All transient DNS were performed for case 4 in table 1, on a grid of square cells with increments $\Delta_x = \Delta_r = 2^{-7}$ in the bulk of the fluid phases and $\Delta_x = \Delta_r = 2^{-8}$ around the liquid–gas interface. The time step Δ_t was dynamically adapted so that $w^\star\,\Delta_t/\Delta_x \leqslant 0.8$ in each cell, whereby $w^\star$ denotes the magnitude of the local dimensional velocity. We have verified that our simulations are grid independent. Results of our transient DNS are presented in appendix A, where they are used to validate our model computations.

The second DNS code allows us to construct travelling-wave solutions of (2.1)–(2.4) based on a pseudo-spectral approach, which we have integrated into the continuation software AUTO07P (Doedel 2008). This has allowed us to verify our numerical continuation results obtained with the WRIBL model (see figure 5*d*). In these travelling-wave DNS, the gas phase is not accounted for, i.e. $\Pi_\mu = \Pi_\rho = 0$, and, thus, we have only applied them to case 3, where the effect of the gas is negligible. The underlying numerical procedure is detailed in appendix B.

2.3. *Linear stability analysis*

Linearizing the WRIBL model (2.5) around the uniform base state $\{d, q_k\} = \{d_0, q_{k0}\}$ and assuming a small-amplitude perturbation $\{d', q_k'\}$,

$$\left.\begin{aligned} d(x,t) &= d_0 + d'(x,t) = d_0 + \hat{d}\exp[\mathrm{i}(\alpha x - \omega t)] \\ q_k(x,t) &= q_{k0} + q_k'(x,t) = q_{k0} + \hat{q}_k \exp[\mathrm{i}(\alpha x - \omega t)] \end{aligned}\right\} \tag{2.10}$$

yields the complex dispersion relation

$$\begin{aligned} DR(\omega,\alpha) \;=\; & 2\pi d_0 \omega\{\varepsilon_{jl}C_{jl} + \varepsilon_{jg}\Pi_\mu C_{jg}\} + \alpha\{\partial_d C_{jl} q_{j0} - \Pi_\mu \partial_d C_{jg} q_{j0}\} \\ & - 2\pi d_0 \alpha^2 M_j \varepsilon_{jl} - \alpha^3 L_j q_{j0} - \mathrm{i}ReWe\{\alpha^2/d_0^2 - \alpha^4\} \\ & + \mathrm{i}Re\{2\pi d_0[\omega^2(S_g - Sl) + \omega\alpha(F_{jl}q_{j0} - F_{jg}q_{j0})] - \alpha^2 G_{jk}\}, \end{aligned} \tag{2.11}$$

where j and k are to be permuted over the phase indicators l and g, ω designates the (complex) wave frequency, α the (complex) wave number, $\varepsilon_{ll} = \varepsilon_{gg} = -1$, and $\varepsilon_{lg} = \varepsilon_{gl} = 1$.

A temporal stability analysis assumes that waves grow self-similarly in their reference frame. This description implies $\alpha \in \mathbb{R}$ and $\omega = \omega_r + \mathrm{i}\omega_i$, where the temporal growth rate ω_i is obtained by solving $DR(\omega, \alpha) = 0$. In figure 2(*a*) we have plotted the thus obtained dispersion curve $\omega_i(\alpha)$ of the temporal growth rate for cases 1, 3 and 4 from table 1. Lines correspond to the model dispersion relation (2.11), and symbols correspond to our own numerical solutions of the Orr–Sommerfeld equations, following the work of Hickox (1971). Agreement between the two data sets is good. Thus, our model is able to accurately represent the linear wave selection.

https://doi.org/10.1017/jfm.2020.267 Published online by Cambridge University Press

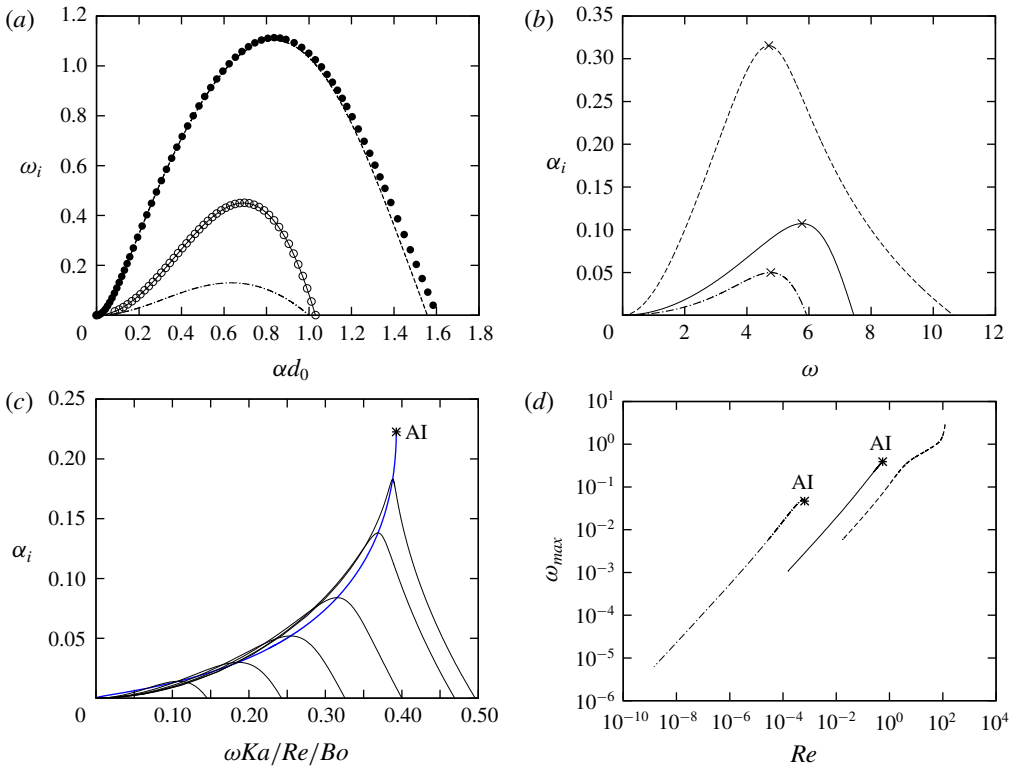


FIGURE 2. Linear instability predictions for three cases from table 1: case 1 (dot–dashed lines, diamonds); case 3 (solid lines, open circles); case 4 (dashed lines, filled circles). The core fluid is subject to an aerostatic pressure gradient $\Psi = 1$. Lines correspond to the model dispersion relation (2.11). (*a*) Temporal growth: $\alpha \in \mathbb{R}$, $\omega = \omega_r + \mathrm{i}\omega_i$ in (2.10). Symbols correspond to the Orr–Sommerfeld solution, following the work of Hickox (1971). (*b*) Spatial growth: $\omega \in \mathbb{R}$, $\alpha = \alpha_r + \mathrm{i}\alpha_i$ in (2.10). Crosses highlight maximal spatial growth. (*c*) Dispersion curves under increasing $Re \in [0.1, 0.54]$. Blue line traces maximum growth rate $\alpha_i(\omega_{max})$. (*d*) Most amplified angular velocity ω_{max} versus Re. Asterisks mark the absolute linear instability (AI) threshold.

In a spatially evolving film, it is more representative to consider the spatial growth rate α_i. We thus solve $DR(\omega, \alpha) = 0$ for $\alpha_i(\omega)$, by assuming that $\omega \in \mathbb{R}$ and $\alpha = \alpha_r + \mathrm{i}\alpha_i$. In figure 2(*b*) we have plotted the thus obtained growth rate dispersion curves $\alpha_i(\omega)$ for the three cases from figure 2(*a*). Crosses mark the point of maximal growth rate and we denote ω_{max} the associated most amplified angular velocity.

In § 3.2 we will characterize occlusion by determining the limit of travelling-wave solutions through numerical continuation. This limit is very sensitive to the wave frequency f. Thus, we focus on the spatially most amplified waves, which are most likely to emerge from linear wave selection in an experiment. For this, we impose the linearly most amplified frequency $f_{max} = 2\pi/\omega_{max}$ in our continuation runs.

To determine f_{max}, which changes with the control parameters varied in these runs, our continuation code was augmented to additionally solve for ω_{max} subject to

$$DR(\omega_{max}, \alpha) = 0, \quad \partial_\omega \alpha_i|_{\omega=\omega_{max}} = 0, \tag{2.12a,b}$$

https://doi.org/10.1017/jfm.2020.267 Published online by Cambridge University Press

where $\partial_\omega \alpha_i$ is obtained from $\partial_\omega DR = 0$. In a given continuation run, the linear stability problem (2.12) is solved for the primary flow $\{q_{l0}, q_{g0}\} = \{\bar{q}_l, \bar{q}_g\}$, which is fixed by the mean flow rates $\bar{q}_l$ and $\bar{q}_g$ of the current travelling-wave solution.

As shown by Camassa *et al.* (2014), the annular falling liquid film can be subject to absolute instability. Thus, we have checked for the absolute instability (AI) threshold in all our continuation runs. In the context of our spatial stability analysis, where $\omega \in \mathbb{R}$, the AI threshold bounds the solutions of (2.12) in terms of the varied control parameter, e.g. Re, because the maximum growth rate $\alpha_i(\omega_{max})$ diverges there. For example, figure 2(*c*) represents the dispersion curves $\alpha_i(\omega)$ for case 3 at different values of Re, increased towards the AI threshold. The latter is marked by an asterisk on the blue curve, which traces the locus of the spatial growth rate maximum $\alpha_i(\omega_{max})$. We point out that ω has been rescaled in figure 2(*c*).

Figure 2(*d*) represents how ω_{max} changes with Re for the three cases from figure 2(*b*). These curves allow us to discern the AI threshold (marked by asterisks) in terms of Re. For case 4 (dashed curve), we have truncated our solution at $Re = 100$, beyond which our nonlinear model predictions are no longer reliable. The AI threshold lies beyond this point but, as we will see, the occlusion bound Re_{max} lies well within the represented range (figure 6*a*).

In our current study, we focus on regimes where $Bo \geqslant 1$. In this case, the AI threshold is always situated beyond the limit of nonlinear travelling-wave solutions and, thus, it does not affect the occlusion bound. However, we will demonstrate that neglecting certain physical effects in the mathematical description, such as axial viscous diffusion (figure 9*b*) or inertia (figure 12*a*), can change this.

3. Results and discussion

In §§ 3.1 and 3.2 we reproduce numerically the visualization experiments of Camassa *et al.* (2014) and demonstrate that the occlusion of a narrow tube by a wavy falling liquid film is caused by surface waves that do not possess a finite-amplitude travelling state. Depending on how these waves emerge in a spatially evolving film, either directly from linear instability (scenario I), or subsequent nonlinear dynamics (scenario II), different occlusion scenarios are possible. In § 3.2 we determine the bounds of these two scenarios based on the numerical continuation of travelling-wave solutions with our model (2.5). We obtain an upper conservative bound Re_{max}, above which occlusion in a naturally evolving film is certain, and a lower conservative bound Re_0, below which occlusion is impossible. These bounds delimit a regime of conditional occlusion, $Re_0 < Re < Re_{max}$, where occlusion is theoretically possible but does not necessarily occur in a real system.

In § 3.7 we demonstrate occlusion scenarios I and II, which are associated with the regimes of certain ($Re > Re_{max}$) and conditional occlusion ($Re_0 < Re < Re_{max}$), by reproducing two of the experiments in Dao & Balakotaiah (2000) with our own spatio-temporal computations. Before that, in §§ 3.3 to 3.6, we establish how different physical effects, i.e. gravity, axial viscous diffusion, inertia and the core gas flow, affect the upper conservative bound Re_{max}, which delimits these two regimes. Except for § 3.6, where we will vary the gas Reynolds number Re_g, our computations have been performed for an aerostatic pressure drop, i.e. $\Psi = 1$. This is most representative of experiments in a quiescent gas.

Parameters for our computations are varied around the four cases listed in table 1, which represent real liquids and plausible values of the tube radius. Case 1 corresponds to figure 3(*a*) in Camassa *et al.* (2014), where the working liquid was

https://doi.org/10.1017/jfm.2020.267 Published online by Cambridge University Press

Case	ρ_l (kg m^{-3})	μ_l (Pa s)	σ (mN m^{-1})	$R^\star$ (mm)	Ka (–)	Π_ρ (–)	Π_μ (–)
1	970	12.9	21.5	5.0	3.3×10^{-3}	1.2×10^{-3}	1.4×10^{-6}
2	1260.7	1.049	64.0	4.765	0.30	0.95×10^{-3}	1.7×10^{-5}
3	1223.9	0.167	65.0	3.175	3.53	0.98×10^{-3}	1.1×10^{-4}
4	900	0.0045	20.0	1.5	121.4	1.3×10^{-3}	4.0×10^{-3}

Case	Re_{max} (–)	Fr (–)	We (–)	Bo (–)	La (–)	Ca (–)	Figures
1	1.91×10^{-4}	2.7×10^{-3}	8.4×10^{-5}	11.06	6.3×10^{-4}	0.37	3–5, 9, 11
2	0.038	0.040	7.1×10^{-3}	4.39	0.35	0.142	5, 15
3	0.39	0.063	7.3×10^{-3}	1.86	9.1	0.028	5, 9, 15, 16, 18
4	18.9	0.42	0.18	0.993	1.3×10^3	0.012	6, 9, 12–14, 17–19

TABLE 1. Representative parameters for our computations. Liquid properties correspond to a high-viscosity silicone oil (case 1), glycerol–water mixtures concentrated at 99 % and 89 % by mass (cases 2 and 3), and a low-viscosity silicone oil (case 4), while the core fluid is air with $\mu_g = 1.8 \times 10^{-5}$ Pa s and $\rho_g = 1.2$ kg m^{-3}. Case 1 corresponds to figure 3(*a*) in Camassa *et al.* (2014), and cases 2 and 3 correspond to experimental runs 20 and 13 in Dao & Balakotaiah (2000). The dimensionless groups are $Bo = \rho_l g \mathcal{L}^2/\sigma$, $Ca = \mu_l \mathcal{U}/\sigma$, $Re = \rho_l \mathcal{U}\mathcal{L}/\mu_l$, $Ka = \sigma \rho_l^{-1} g^{-1/3} \mu_l^{-4/3}$, $La = \sigma \rho_l \mathcal{L}/\mu_l^2$, $We = \rho_l \mathcal{U}^2 \mathcal{L}/\sigma$ and $Fr = \mathcal{U}/\sqrt{g\mathcal{L}}$, where $\mathcal{L} = R^\star$ and $\mathcal{U} = q_{l0}^\star/\pi/\mathcal{L}^2$, $q_{l0}^\star$ designating the dimensional nominal liquid flow rate. We denote by Re_{max} the upper conservative occlusion bound (see e.g. figures 5*a* and 5*b*).

a high-viscosity silicone oil. Cases 2 and 3 correspond to experimental runs 20 and 13 in Dao & Balakotaiah (2000), where glycerol–water mixtures concentrated at 99 % and 89 % by mass were used. Finally, case 4 concerns a liquid film of low-viscosity silicone oil. The four cases cover a considerable range of the Laplace number $La = \sigma \rho_l R^\star/\mu_l^2$, which relates capillarity to viscous drag, and the Reynolds number, which we have quantified with Re_{max}. We see that inertia, which drives the Kapitza instability, is significant for case 4. For this case, which is the most challenging, we have validated our model computations with transient DNS in appendix A (comparisons with travelling-wave DNS, for case 3, are reported in figure 5*d*).

3.1. *Nature of the surface waves that cause occlusion*

Camassa *et al.* (2014) performed occlusion experiments in an $R^\star = 0.5$ mm and $L^\star = 400$ mm transparent tube using high-viscosity silicone oil (case 1 in table 1). In their figure 3, the authors produce photographs of the wavy falling liquid film at different Re beyond the experimental occlusion threshold, allowing us to discern the nature of the surface waves that cause occlusion. We have reproduced three of these experiments with spatio-temporal computations based on our model (2.5) on a long domain using inlet/outlet conditions (see § 2.1). Experimental noise was mimicked through the noisy inlet perturbation (2.6), where we set $\epsilon_1 = 0$, and tuned ϵ_2 to match the spatial evolution of surface waves in the experiments (when decreasing/increasing ϵ_2, the region of linear growth of surface waves is stretched/compressed in streamwise direction and this shifts the emergence of nonlinear effects, such as occlusion, downstream/upstream). In figure 3 we show snapshots of these computations, which are to be directly compared to figures 3(*a*), 3(*b*) and 3(*c*) in Camassa *et al.* (2014).

https://doi.org/10.1017/jfm.2020.267 Published online by Cambridge University Press

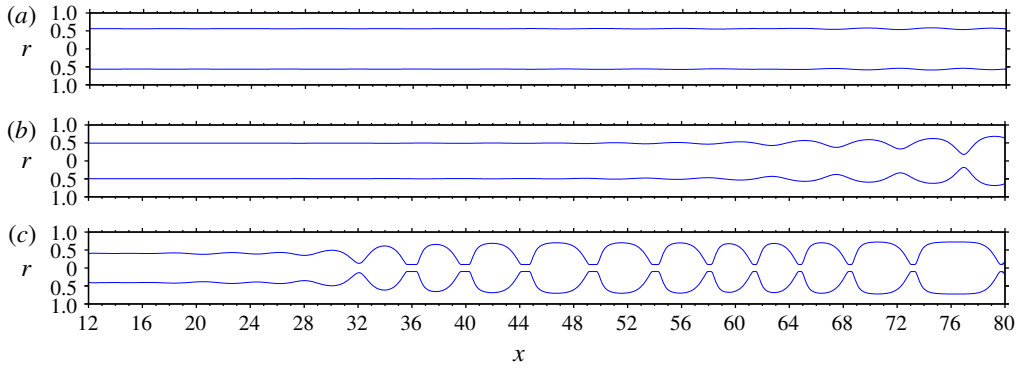


FIGURE 3. Spatio-temporal computations of the experiments in figures 3(*a*), 3(*b*) and 3(*c*) of Camassa *et al.* (2014), which were performed in an $L^\star = 400$ mm tube. Parameters correspond to case 1 in table 1. Computations were performed with our model (2.5) using inlet/outlet conditions and the noisy inlet perturbation (2.6), where we set $\epsilon_1 = 0$ and adjusted ϵ_2 to match the experimental wave growth. (*a*) $Re = 2.3 \times 10^{-4}$, $q^\star_{l0} = 4.8 \times 10^{-2}$ cm^3 s^{-1}, $\epsilon_2 = 0.0002$; (*b*) $Re = 3.2 \times 10^{-4}$, $q^\star_{l0} = 6.7 \times 10^{-2}$ cm^3 s^{-1}, $\epsilon_2 = 0.00005$; (*c*) $Re = 4.5 \times 10^{-4}$, $q^\star_{l0} = 9.4 \times 10^{-2}$ cm^3 s^{-1}, $\epsilon_2 = 0.0001$.

Agreement with the experimental snapshots is good. In particular, the wavelength of the four distinct surface waves at the tube outlet in figure 3(*b*) is predicted accurately by our computations. Also, the number of gas bubbles (eleven) in figure 3(*c*), which result from successive occlusion events, agrees with the experiment. Figure 3(*c*) and the supplementary movie M1 allow us to discern the actual mechanics of occlusion. Surface waves in the upstream portion of the tube grow spatially until their crests reach the tube axis, whereupon individual bubbles of the gas core are pinched off. Our model accurately predicts the length scale of the pinch-off process in comparison with the experiment. We stress that figure 3(*c*) is a snapshot and that the occlusion point shifts up and down the tube intermittently as a result of the noisy wave spectrum imposed through the inlet condition. These results show that our model captures accurately the wave dynamics leading up to occlusion, and this is the focus of our current study. However, the physics of the liquid plugs resulting from occlusion is captured only very crudely by the numerical core radius limitation introduced in § 2.1. For example, the shape of the gas bubbles in figure 3(*c*) is quite different from that in the experiment and their length evolves as they travel downstream (see also supplementary movie M1). First results reported in appendix E suggest that these shortcomings can be alleviated with our improved WRIBL model. But the exact shape of liquid plugs can never be fully captured in the context of lubrication theory, as the film surface slope diverges at their edges.

We now focus on figure 3(*a*), where *Re* is closest to the experimental occlusion threshold. For this case, Camassa *et al.* (2014) observed occlusion only after having switched to a longer $L^\star = 1$ m tube. Because of the small spatial growth rate, distinguishable surface waves emerged only very close to the outlet of the shorter $L^\star = 400$ mm tube, and their amplitude was insufficient to cause occlusion there. Our computation in figure 3(*a*) exhibits the same behaviour.

We have also reproduced numerically the experiment in the $L^\star = 1$ m tube and a snapshot of our computation is represented in figure 4(*a*). It confirms that occlusion does indeed occur, in the region $x \geqslant 130$. Occlusion results from unbounded spatial

https://doi.org/10.1017/jfm.2020.267 Published online by Cambridge University Press

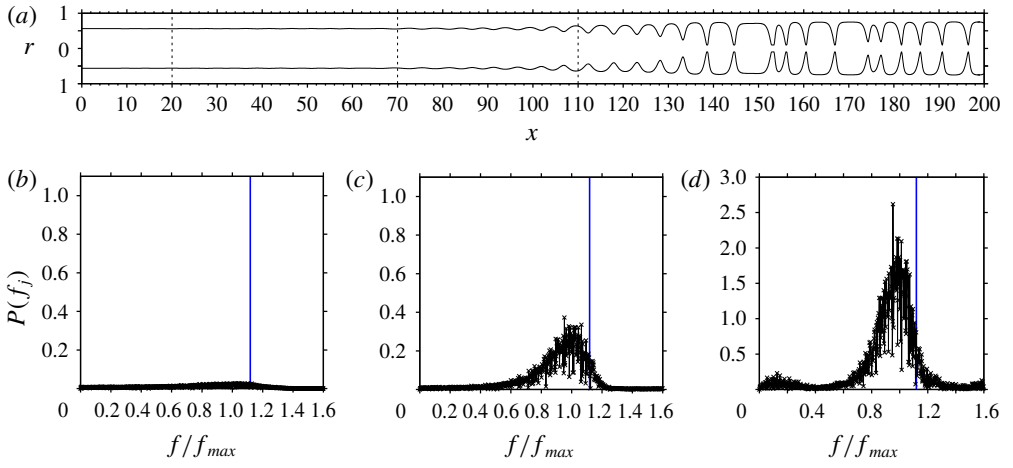


FIGURE 4. Nature of the prevailing surface waves that cause occlusion. Spatio-temporal computation reproducing the second version of the experiment in figure 3(*a*) of Camassa *et al.* (2014), which was performed in a longer $L^\star = 1$ m tube: case 1 in table 1, $Re = 2.3 \times 10^{-4}$. (*a*) Snapshot of the computed film profile, showing individual surface waves that cause occlusion in the region $x \geqslant 130$. (*b–d*) Frequency spectra at different streamwise locations leading up to the occlusion region (marked by dashed lines in panel *a*): (*b*) $x = 20$; (*c*) $x = 70$; (*d*) $x = 110$. Vertical blue lines at $f/f_{max} = 1.12$ mark the limit of travelling-wave solutions determined by numerical continuation (see figure 6*b*). Here f_{max} designates the spatially most amplified frequency of linear waves.

growth of the prevailing surface waves, and figures 4(*b*) to 4(*d*) show how the latter emerge from the noisy inlet condition. In these panels, we have represented the single-sided amplitude spectrum $P(f_j)$ of the discrete Fourier transform $F(f_j)$ applied to core radius time series $d(t_k)$ recorded at different streamwise positions x (marked by dashed lines in figure 4*a*), leading up to the occlusion region

$$P(f_j) = (2/N)F(f_j)\ \forall\, j \leqslant N/2+1, \quad F(f_j) = \sum_{k=0}^{N} d(t_k)\exp(\mathrm{i}2\pi j/Nk), \tag{3.1a,b}$$

where $N = 1.8 \times 10^6$ is the number of (equidistant) sampling points t_k with which we have recorded the time series $d(t_k)$ over a duration $T = 9.1 \times 10^4$, and $f_j = (j/N)/T$ are the frequencies of the discrete spectrum. At the most downstream location (figure 4*d*), the spectrum is organized around the spatially most amplified frequency of linear waves f_{max} in the form of a quite narrow peak. This peak lies beyond the limit $f/f_{max} = 1.12$ for the existence of travelling-wave solutions at the considered Reynolds number $Re = 2.3 \times 10^{-4}$, which is highlighted by vertical blue lines in figures 4(*b*), 4(*c*) and 4(*d*). This limit has been determined by numerical continuation of travelling-wave solutions, which we will discuss in the next subsection (it is marked by an asterisk in figure 5*b*). We will see that higher frequency (shorter) waves are safe from and lower frequency (longer) waves are prone to occlusion.

By way of numerical continuation, Camassa *et al.* (2014) were the first to show that the existence of travelling-wave solutions is bounded. By increasing Re at fixed wavelength, the authors found a limit point beyond which travelling-wave solutions cease to exist. They conjectured that the loss of such solutions signals occlusion in

https://doi.org/10.1017/jfm.2020.267 Published online by Cambridge University Press

an actual experiment. However, the authors cautioned that further work was needed to verify this conjecture. This work was initiated by Camassa *et al.* (2016), but their model did not account for axial viscous diffusion. Our computations in figures 3 and 4 provide further validation, by taking into account this effect, which greatly improves agreement of our model predictions with the experiments of Camassa *et al.* (2014), as a result of the high viscosity of the working liquid. For example, when running the computation in figure 4(*a*) without axial viscous diffusion, we did not observe any occlusion over the entire experimental tube length (see figure 21 in appendix D), which is in qualitative contradiction to the experiments. Also, we will show in § 3.4 that neglecting axial viscous diffusion increases Re_{max} by 74 % for this liquid (figure 9*a*), moving it far beyond the experimental occlusion limit, as quantified in terms of Re.

Figure 4 proves that the occlusion of a narrow tube by a wavy falling liquid film is caused by surface waves that lie beyond the limit of travelling-wave solutions. Thus, occlusion can be characterized based on the existence span of such solutions and we proceed to this in the following subsection.

3.2. *Travelling waves: regimes of certain, conditional and impossible occlusion*

The frequency of travelling waves determines their amplitude, which is well known for planar falling liquid films (Nosoko *et al.* 1996) and also holds in our cylindrical configuration. At a given value of Re, the smaller the wave frequency, the greater the wave amplitude. Consequently, low-frequency travelling waves are more prone to occlusion than high-frequency waves. This effect was demonstrated by Camassa *et al.* (2016) and Ding *et al.* (2019) with a first-order asymptotic model and a lubrication model, respectively. Using our model (2.5), we quantify it for the real liquids studied here (cases 1–4 in table 1), which require a more complicated modelling approach.

Figure 5(*a*) represents curves of travelling-wave solutions for case 1 in terms of the minimal core radius d_{min}, as obtained by varying the liquid Reynolds number Re. On each curve, we have fixed the wave frequency f to a certain fraction f/f_{max} of the spatially most amplified frequency f_{max}, which we determine through the approach outlined in § 2.3. All curves display a limit point in terms of Re, beyond which there are no travelling-wave solutions. The existence of such a limit point was discovered by Camassa *et al.* (2014), who imposed a constant wavelength in their continuation. This wavelength was too long compared to their experiments, whereas we see here that accounting for the correct wavelength/frequency is quite important. Indeed, the limit point of the curves in figure 5(*a*) varies greatly with f/f_{max}. The lower the wave frequency, the smaller the limit value of Re, the more danger of occlusion.

We now introduce the upper conservative occlusion bound Re_{max}, which corresponds to the limit point (LP) of the solid line representing the spatially most amplified travelling waves, i.e. $f/f_{max} = 1$. For $Re > Re_{max}$, the linearly most amplified surface waves, which are most likely to emerge in an experiment, do not possess travelling states and occlusion is certain to occur in a naturally evolving film. The experiment of Camassa *et al.* (2014), which we have reproduced numerically in figure 4, corresponds to this regime. Occlusion in this case occurs through scenario I, which we will discuss further in § 3.7 based on spatio-temporal computations.

Figure 5(*b*) explains the meaning of the upper occlusion bound Re_{max} in a different way, by illustrating the effect of the wave frequency f at fixed Re. The dashed blue line represents the linear spatial growth rate α_i at $Re = Re_{max}$ (right abscissa), while all other curves represent travelling-wave solutions (left abscissa) at different Re. These

https://doi.org/10.1017/jfm.2020.267 Published online by Cambridge University Press

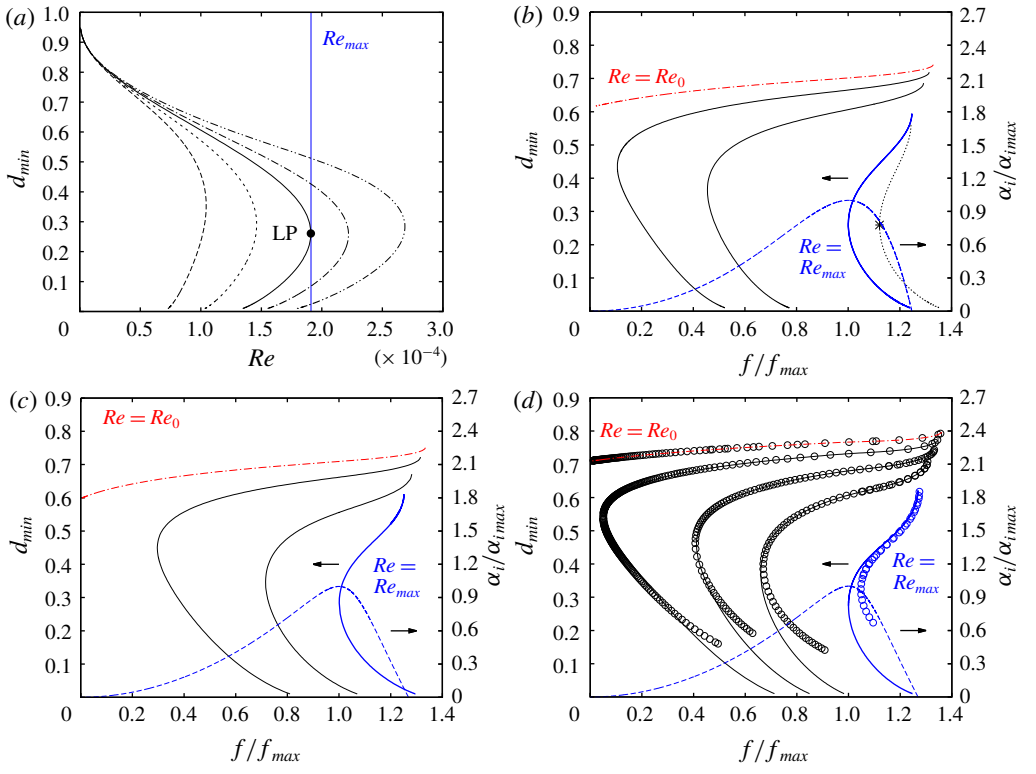


FIGURE 5. Limits of travelling-wave solutions obtained from numerical continuation with our model (2.5). Cases 1 (panels *a*,*b*), 2 (panel *c*) and 3 (panel *d*) in table 1. (*a*) Continuation of Re at wave frequency $f/f_{max} = 0.5$ (long dashes), 0.8 (short dashes), 1 (solid), 1.1 (dot–dashed), and 1.2 (dot–dot–dashed). The vertical blue line marks the limit point for spatially most amplified linear waves, where $f = f_{max}$ and $Re = Re_{max}$. (*b–d*) Frequency dependence at $Re = \text{const}$. Dashed blue: linear spatial growth rate α_i at $Re = Re_{max}$ (right abscissae). Other: travelling-wave solutions at $Re = \text{const}$. (left abscissae). (*b*) Case 1: $Re = Re_0 = 6 \times 10^{-5}$ (dot–dashed red), $Re = 7.5 \times 10^{-5}$, 1×10^{-4} (thin solid), $Re = Re_{max} = 1.91 \times 10^{-4}$ (thick solid blue), and $Re = 2.3 \times 10^{-4}$ (dotted with asterisk). (*c*) Case 2: $Re = Re_0 = 0.012$ (dot–dashed red), $Re = 0.016$, 0.025 (thin solid), and $Re = Re_{max} = 0.038$ (thick solid). (*d*) Case 3: $Re = Re_0 = 0.075$ (dot–dashed red), $Re = 0.1$, 0.14, 0.2 (thin solid), and $Re = Re_{max} = 0.393$ (thick solid). Open circles correspond to data obtained with our own travelling-wave DNS (see § 2.2).

curves all display a limit point in terms of f. The dotted line marked by an asterisk corresponds to the experiment of Camassa *et al.* (2014) numerically reproduced in figure 4, where $Re = 2.3 \times 10^{-4}$. The thick blue solid line corresponds to the upper occlusion bound $Re = Re_{max} = 1.9 \times 10^{-4}$ and its limit point thus coincides with the maximum of the growth rate dispersion curve $\alpha_i(f)$. We stress that determining Re_{max} requires simultaneously computing the most amplified wave frequency f_{max} in our numerical continuations, as described in § 2.3. This had not been attempted in the previous studies of Camassa *et al.* (2014) and Ding *et al.* (2019).

Reducing Re below Re_{max} moves the limit point of travelling-wave solutions to lower values of f. Thus, the occlusion range is increasingly confined to (very long) waves of very low frequency, until it vanishes completely at $Re = Re_0$ (red dot–dashed

https://doi.org/10.1017/jfm.2020.267 Published online by Cambridge University Press

curve in figure 5*b*). This limit, the existence of which was discovered by Ding *et al.* (2019), constitutes a lower conservative occlusion bound. When $Re < Re_0$, occlusion is impossible, no matter how long the waves. In a real system, it is conceivable that wave coalescence events can produce local overshoots leading to occlusion even when $Re < Re_0$. However, we have not observed this in our computations of spatially evolving films (see figures 16*b* and 17*c*). The value Re_0 being very low for all studied liquids, inertia is weak and significant overshoots are unlikely.

Based on the conservative occlusion bounds Re_0 and Re_{max}, we delimit a region of conditional occlusion, $Re_0 < Re < Re_{max}$ (between the red dot–dashed and thick solid blue lines in figure 5*b*), where occlusion is theoretically possible, for long enough waves, but does not necessarily occur in a real system. That depends on whether the required waves actually develop in a spatially evolving film. And, in particular, whether the tube is long enough to accommodate the nonlinear wave dynamics required to produce them. In § 3.7 we will demonstrate that occlusion in this regime occurs through scenario II, i.e. wave coarsening triggered by secondary instability, which shifts surface waves down the ascending branch of the dispersion curve towards increasingly low frequencies.

In figure 5(*a*), the limit point is a turning point, where two solution branches meet. As suggested by Camassa *et al.* (2014), we have checked their stability using transient periodic simulations with imposed Ψ started from selected travelling-wave solutions. In these computations, numerical noise is responsible for perturbing the flow. A full-fledged formal stability analysis, such as the one performed by Camassa *et al.* (2016) based on the first-order model of Camassa *et al.* (2014), is outside the scope of our current study. We find that the lower solution branch is entirely unstable. As this branch does not connect to the flat-film primary flow $d_{min} = d_{max} = 1$, the solutions thereon are thus highly unlikely in an experiment. Conversely, the upper branch is stable, at least with respect to periodic perturbations. However, wave trains of high-frequency travelling waves on falling liquid films are subject to secondary subharmonic and sideband instabilities that rely on wave interaction and lead to coalescence events (Liu & Gollub 1993). We have found that this triggers occlusion scenario II, which we will demonstrate in § 3.7. Finally, when starting a periodic transient computation from a flat-film initial condition beyond the limit of travelling-wave solutions, the outcome is indeed occlusion, which we have checked (and validated with transient DNS) in appendix A (see figures 19*a* and 19*b*).

Figures 5(*c*) (case 2), 5(*d*) (case 3) and 6 (case 4) report the occlusion bounds Re_{max} and Re_0 for the other three cases from table 1. In figure 5(*d*) we have represented with open circles additional results obtained with our own travelling-wave DNS (see § 2.2), evidencing gratifying agreement with our WRIBL model predictions. Overall tendencies in these graphs are the same as for case 1. For case 4 (low-viscosity silicone oil), where the Kapitza instability is relevant, there is an additional feature. In figure 6(*a*), the continuation curves of d_{min} (Re, $f = \text{const.}$) at high frequencies, e.g. the dot–dot–dashed curve at $f/f_{max} = 1.2$, exhibit two lobes that are each associated with a limit point. Wave profiles corresponding to these highlighted points LP1 and LP2 are represented in figure 6(*c*). We see that the main wave hump is preceded by a small precursory ripple. Such so-called capillary ripples can produce multiplicity of solutions in falling liquid films, when they are close enough to interact with the following wave hump (Kalliadasis *et al.* 2012). By contrast, the dashed curves in figure 6(*a*), which pertain to low-frequency waves, each display only a single limit point. In figures 6(*d*) and 6(*e*) we show the corresponding wave profiles at those points. We see in figures 6(*c*), 6(*d*) and 6(*e*) that lower wave frequencies are associated with longer wavelengths, which we have implicitly assumed up until now.

https://doi.org/10.1017/jfm.2020.267 Published online by Cambridge University Press

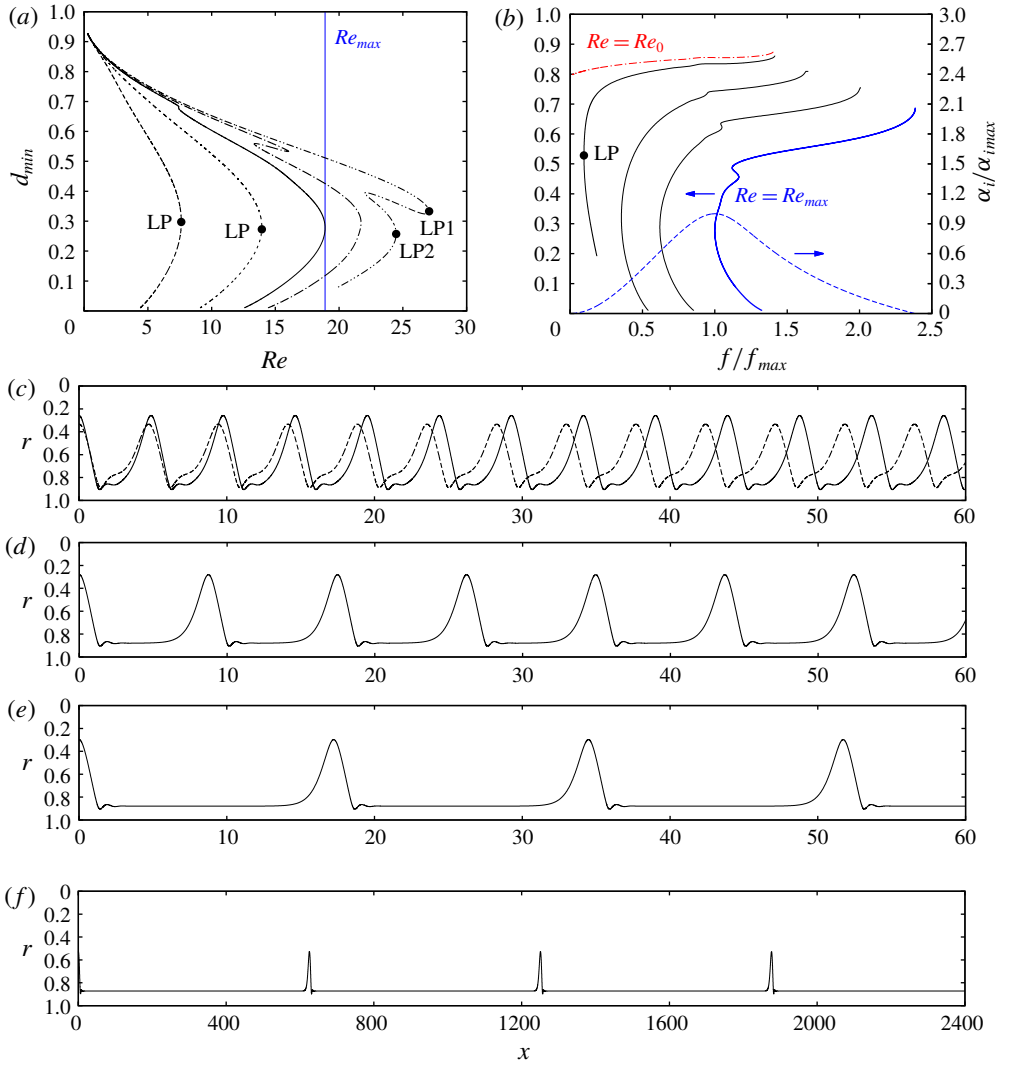


FIGURE 6. Limits of travelling-wave solutions for case 4 in table 1. (*a*) Continuation of Re at constant wave frequency $f/f_{max} = 0.5$ (long dashes), 0.8 (short dashes), 1 (solid), 1.1 (dot–dashed) and 1.2 (dot–dot–dashed). (*b*) Frequency dependence at $Re = \text{const}$. Dashed: linear spatial growth rate α_i at $Re = Re_{max} = 18.9$ (right abscissa). Other: travelling-wave solutions (left abscissa) at $Re = Re_0 = 1.5$ (dot–dashed red), $Re = 2$, 5, 10 (thin solid), and $Re = Re_{max}$ (thick blue). (*c–e*) Film profiles for LPs marked by filled circles in panel *a*; (*c*) $f = 1.2f_{max}$. Solid, LP1; dashed, LP2; (*d*) $f = 0.8f_{max}$; (*e*) $f = 0.5f_{max}$; (*f*) profile for marked LP in panel (*b*).

Finally, figure 6(*f*) represents the wave profile corresponding to the limit point marked by a filled circle on the $Re = 2$ curve in figure 6(*b*). This curve lies in the region of conditional occlusion, $Re_0 < Re < Re_{max}$ ($Re_0 = 1.5$, $Re_{max} = 18.9$). However, based on the wavelength of the waves in figure 6(*f*), which span about 600 times the tube radius, it becomes clear that quite particular conditions can be required to cause occlusion in this regime. This underlines the conservative nature of the lower occlusion bound Re_0.

https://doi.org/10.1017/jfm.2020.267 Published online by Cambridge University Press

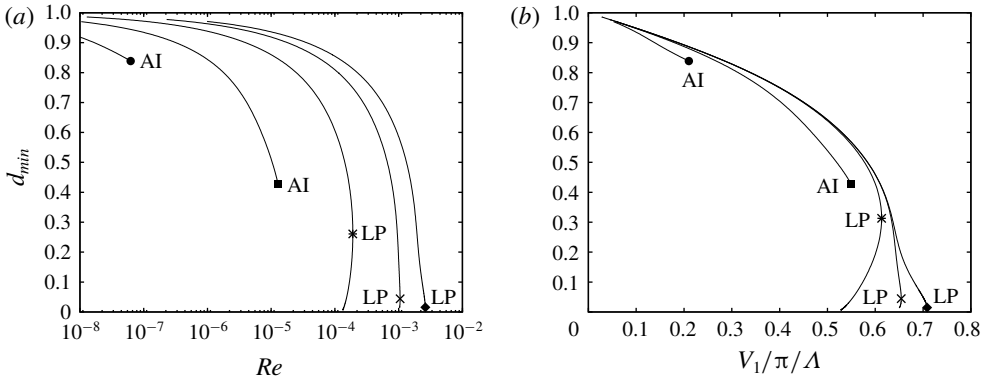


FIGURE 7. Delay of occlusion by increasing the Bond number $Bo = \rho_l g R^{\star 2}/\sigma$ at constant Laplace number: $La = \sigma\rho_l R^{\star}/\mu_l^2 = 6.27 \times 10^{-4}$ (case 1). Travelling-wave solutions at $f = f_{max}$. Symbols mark onset of absolute linear instability (AI) or limit points (LP). The limit points correspond to the upper occlusion bound Re_{max}. Circles, $Bo = 0.1$; squares, $Bo = 1$; asterisks, $Bo = 11.1$ (case 1); crosses, $Bo = 50$; diamonds, $Bo = 100$. (*a*) Minimal core radius d_{min} versus liquid Reynolds number. (*b*) Minimal core radius versus liquid holdup.

In summary, due to the frequency dependence of travelling-wave solutions demonstrated in figures 5(*b*), 5(*c*), 5(*d*) and 6(*b*), three characteristic regimes can be delimited: (i) impossible occlusion, when $Re < Re_0$; (ii) conditional occlusion, when $Re_0 < Re < Re_{max}$; and (iii) certain occlusion, when $Re > Re_{max}$. In § 3.7 we will characterize these regimes with spatio-temporal computations and demonstrate the associated occlusion scenarios I and II. On the other hand, the frequency dependence of travelling-wave solutions opens the possibility of using coherent inlet forcing to prevent occlusion. By forcing regular waves of sufficiently high frequency, occlusion can be avoided versus a noise-driven wave evolution. We demonstrate this idea in § 3.8 based on spatio-temporal computations. In the next sections, § 3.3 to § 3.6, we first proceed to establish how different physical effects, i.e. gravity, axial viscous diffusion, inertia and the core gas flow, affect the upper conservative occlusion bound Re_{max}.

3.3. *Role of gravity*

The upper occlusion bound Re_{max} can be significantly delayed by increasing the relative strength of gravity versus capillarity. We have quantified this by varying the Bond number $Bo = \rho_l g R^{\star 2}/\sigma$ over several orders of magnitude at constant Laplace number $La = 6.3 \times 10^{-4}$. This value of La corresponds to the high-viscosity silicone oil (case 1), where inertia is always negligible.

Figure 7(*a*) represents travelling-wave solutions for different values of Bo. On each curve we have imposed the frequency f_{max} of the most amplified spatially growing linear waves. All curves exhibit a limit value for the liquid Reynolds number Re. For $Bo \ll 1$, where the Plateau–Rayleigh instability dominates, this limit is dictated by the onset of absolute instability, as discussed in figures 2(*c*) and 2(*d*). Beyond this point, prevailing waves are no longer characterized by the most amplified spatially growing linear waves and f_{max} is no longer defined. The solution curves stop abruptly. Occlusion in this regime is caused by absolute instability of the primary flow. This regime is not the focus of our study.

https://doi.org/10.1017/jfm.2020.267 Published online by Cambridge University Press

We focus on $Bo \geqslant 1$, for which the solution curves in figure 7(*a*) are bounded by a limit point, as discussed in figure 5(*a*). This limit point marks the upper occlusion bound Re_{max}, which increases significantly with increasing Bo, while the minimal core radius d_{min} at LP significantly diminishes. The first observation is in line with the experiments of Dao & Balakotaiah (2000), who reported Re at the experimental occlusion onset for different liquids and tube radii but had no access to the wave dynamics. The authors also outlined an approach for predicting occlusion based on travelling waves, which relied on the conjecture that the wave height always reaches the tube radius as Re is increased towards the occlusion limit. Based on our results in figure 7(*a*), this conjecture only holds when Bo is extremely large. Otherwise, travelling-wave solutions are lost well before their height attains the tube radius.

In figure 7(*b*) we have replotted our results from figure 7(*a*) in terms of the liquid hold-up $V_l/\pi/\Lambda$. We see that the maximally achievable liquid hold-up increases significantly with Bo. This again is in line with the experiments of Dao & Balakotaiah (2000), who had observed that the mean film thickness $\bar{h}$ at occlusion is significantly greater than in the gravity-free Plateau–Rayleigh configuration (Gauglitz & Radke 1988).

The variation of Bo in figure 7 amounts to varying the gravitational acceleration for constant liquid and tube radius. Of course, it is either very difficult (low Bo range, microgravity experiments) or impossible (high Bo range) to realize the displayed range of variation $0.1 \leqslant Bo \leqslant 100$ practically. A more practicable way to quantify the desired effect is to increase the tube radius R for a constant liquid. This amounts to increasing Bo at constant $Ka = \sigma \rho_l^{-1} g^{-1/3} \mu_l^{-4/3}$. We have performed such computations for $Ka = 3.3 \times 10^{-3}$, corresponding to the high-viscosity silicone oil (case 1). Results are represented in figures 8(*a*) and 8(*b*), and these display the same overall behaviour as figure 7.

The delay of Re_{max} results from a gravity-induced streamwise distortion of surface waves, which favours variations in (stabilizing) axial interface curvature over variations in (destabilizing) azimuthal curvature. Figure 8(*c*) illustrates this distortion, which is marked by a compression of the leading wave front and an elongation of the trailing front. The different surface profiles represented correspond to the absolute instability thresholds and limit points highlighted in figure 8(*a*). Figure 8(*d*) represents corresponding profiles of the axial curvature $\partial_{xx} d$. The variation in (stabilizing) axial curvature $\partial_{xx} d$ around the wave crest (marked by a symbol) significantly increases in magnitude with increasing Bo. This allows us to counter a larger variation in (destabilizing) azimuthal curvature, and, thus, to saturate waves of greater amplitude.

The saturation mechanism was identified by Frenkel *et al.* (1987) for pressure-driven core annular flows, where it is due to a viscous interfacial shear stress, and demonstrated experimentally for falling liquid films on cylindrical fibres by Quéré (1990). In both studies, the saturation took hold in the weakly nonlinear regime, limiting waves to a very small amplitude. Thus, it was perceived as suppressing macroscopically visible waves altogether. In our case, the mechanism takes hold in the strongly nonlinear regime, allowing us to saturate travelling waves of greater amplitude as Bo is increased.

The role of gravity is kinematic, i.e. it makes initial surface elevations travel faster than surface depressions (Dietze 2016), and this produces the distortion of wave fronts observed in figure 8(*c*). We point out that this effect was precluded in Jensen (2000), where surface waves were constructed in the form of perfectly symmetrical unduloids.

https://doi.org/10.1017/jfm.2020.267 Published online by Cambridge University Press

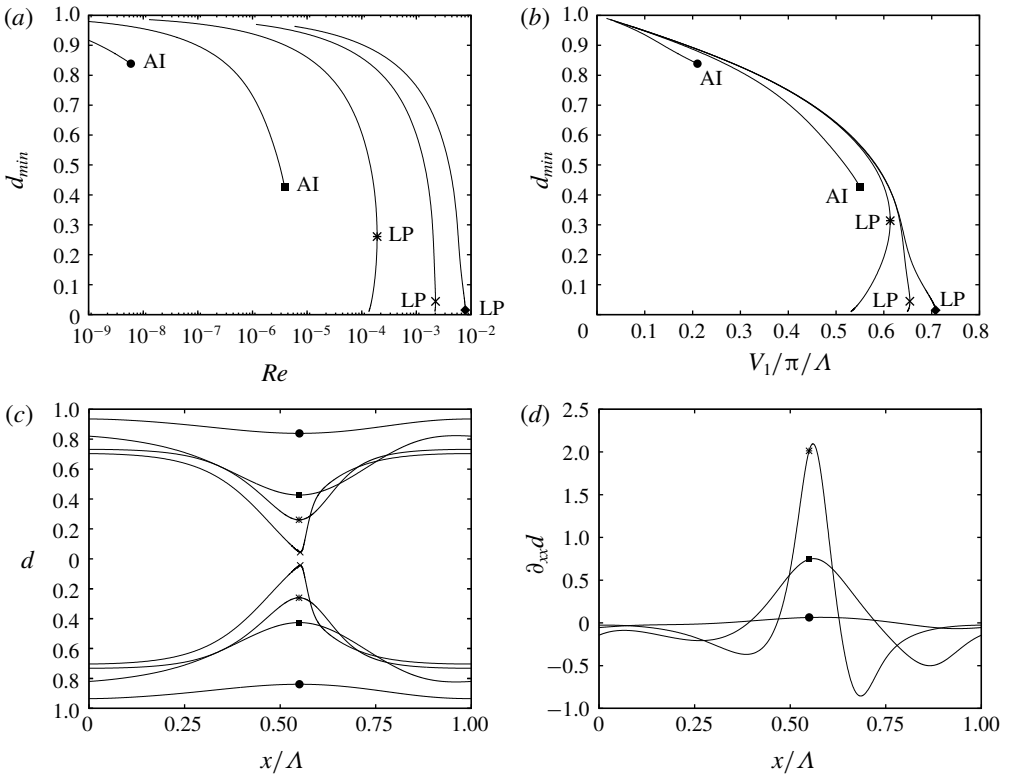


FIGURE 8. Delay of occlusion by increasing the Bond number Bo at constant Kapitza number: $Ka = \sigma\rho_l^{-1}g^{-1/3}\mu_l^{-4/3} = 3.29 \times 10^{-4}$ (case 1). This amounts to increasing the tube radius $R^\star$ while maintaining constant fluid properties. See figure 7 for symbol attributions. (*a*) Minimal core radius d_{min} versus liquid Reynolds number. (*b*) Minimal core radius versus liquid holdup. (*c*) Surface profiles at AI and LP. (*d*) Corresponding profiles of axial curvature $\partial_{xx}d$.

3.4. *Role of axial viscous diffusion*

Axial viscous diffusion, emanating from the $\partial_{xx}u$ term in (2.1), is represented in our model (2.5) through the terms with coefficients J_j, K_j, L_j and M_j. These terms appear when the underlying long-wave expansion is performed up to second order. This was not done in the previous modelling works of Trifonov (1992), Camassa *et al.* (2014, 2017), Zhou *et al.* (2016), Liu & Ding (2017) and Ding *et al.* (2019). So, the question is whether retaining these terms is worth the effort. We have checked this in figures 9(*a*), 9(*b*) and 9(*d*), representing travelling-wave solutions for cases 1, 3 and 4. The three cases span a wide range of the capillary number $Ca = \mu_l\mathcal{U}/\sigma$, which relates viscous to capillary stresses, and which quantifies the relevance of axial viscous diffusion.

In figure 9 solid lines correspond to the full model (2.5) and dot–dashed lines to the limit $J_i = K_i = L_i = M_i = 0$. Furthermore, we distinguish two types of continuations. On the blue curves, which contain no symbols, we have fixed the wavelength $\Lambda = 12.56$. On the black curves with symbols, we have imposed the spatially most amplified frequency of linear waves $f = f_{max}$. In that case, axial viscous diffusion may affect the solution both nonlinearly and linearly (via wave selection), but the latter effect is negligible for the cases considered here. By comparing the solid and dashed curves in

https://doi.org/10.1017/jfm.2020.267 Published online by Cambridge University Press

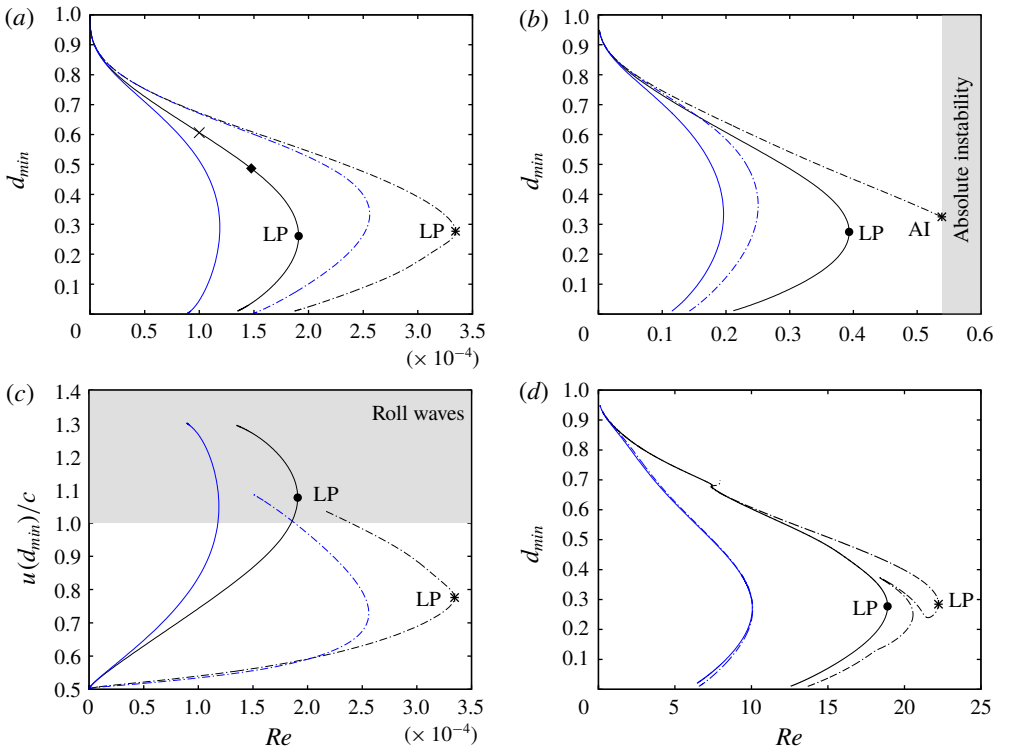


FIGURE 9. Precipitation of occlusion due to axial viscous diffusion. Cases 1, 2 and 3. Circles/asterisks mark limit points (LP) and absolute instability (AI) onset. Solid lines, full model (2.5); dot–dashed lines, no axial viscous diffusion, $J_j = K_j = L_j = M_j = 0$ in (2.5) and (2.11); black curves with symbols, $f = f_{max}$; blue lines without symbols, $\Lambda = 12.56$. The capillary number Ca scales the observed effect. (*a*,*c*) Case 1: $Ca = 0.37$. The crosses and diamonds mark points used in figure 10. Panel (*c*) represents the ratio of interfacial fluid velocity $u(d_{min})$ to wave speed c. The grey region marks the existence of roll waves $u(d_{min}) > c$. (*b*) Case 3: $Ca = 0.028$. In the grey region, the primary flow is absolutely unstable. (*d*) Case 4: $Ca = 0.012$.

figures 9(*a*), 9(*b*) and 9(*d*), we see that axial viscous diffusion precipitates occlusion in general and Re_{max} in particular and this effect increases with Ca.

For the high-viscosity silicone oil (figure 9(*a*), case 1: $Ca = 0.37$), accounting for axial viscous diffusion greatly reduces Re_{max}, i.e. from $Re_{max} = 3.3 \times 10^{-4}$ to $Re_{max} = 1.9 \times 10^{-4}$ (compare dot–dashed and solid black lines with symbols). It is insightful to compare these values to the experimental occlusion bound, which was observed by Camassa *et al.* (2014) between $Re = 1.6 \times 10^{-4}$ and $Re = 2.3 \times 10^{-4}$ for their 1 m long tube. Linear interpolation based on their table 1 and figure 11 yields a value of $Re = 2.2 \times 10^{-4}$, which is not much greater than our Re_{max} prediction with ($Re_{max} = 1.9 \times 10^{-4}$) but much smaller than our prediction without axial viscous diffusion ($Re_{max} = 3.3 \times 10^{-4}$). Interestingly, when basing the comparison on the mass-equivalent core radius $d_m = (L^{-1} \int_0^L d^2 \, \mathrm{d}x)^{1/2}$, which was also measured by Camassa *et al.* (2014), our two predictions ($d_m^\star = 0.31$ cm versus $d_m^\star = 0.25$ cm) lie equally close to the experimental value $d_m^\star = 0.28$ cm. This explains why Camassa *et al.* (2014, 2016) observed good agreement in terms of this parameter, although

https://doi.org/10.1017/jfm.2020.267 Published online by Cambridge University Press

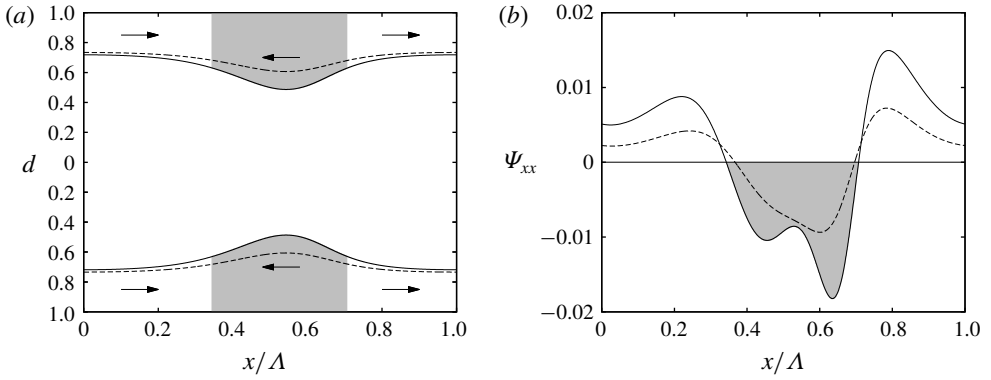


FIGURE 10. Mechanism delaying occlusion due to axial viscous diffusion. Data correspond to the two solution points marked by a cross and a diamond in figure 9(*a*). Solid lines: diamond in figure 9(*a*), $Re = 1.47 \times 10^{-4}$; dashed lines: cross in figure 9(*a*), $Re = 1.0 \times 10^{-4}$. (*a*) Surface profiles with zones of negative (grey) and positive (white) Ψ_{xx}. (*b*) Normalized differential normal axial viscous stress Ψ_{xx} according to (3.2). Axial normal viscous stresses counteract gravity in the wave fronts, tending to steepen the trailing and flatten the leading wave front.

their model did not account for axial viscous diffusion. Finally, we point out that the corresponding values of the primary-flow core radius d_0, which is more representative of the flat film portion in the upper part of the experimental tube, are $d_0^\star = 0.29$ cm with and $d_0^\star = 0.24$ cm without axial viscous diffusion.

For case 3 (figure 9*b*, $Ca = 0.028$), which corresponds to experimental run 13 in Dao & Balakotaiah (2000), axial viscous diffusion dictates even the nature of the occlusion mechanism. For the continuation at $f = f_{max}$ (black lines with symbols in figure 9*b*), occlusion is caused by absolute linear instability (AI) when axial viscous diffusion is neglected (dot–dashed line), and by nonlinear loss of travelling-wave solutions (LP) when it is taken into account (solid line).

For the lowest Ca (figure 9*d*, case 4: $Ca = 0.012$), neglecting axial viscous diffusion does not meaningfully affect Re_{max}. It is, however, responsible for the formation of a second lobe on the black dot–dashed curve marked by an asterisk, which results from a change in the number of precursory ripples, as discussed with respect to figures 6(*a*) and 6(*c*).

The nonlinear mechanism by which axial viscous diffusion precipitates occlusion is illustrated in figure 10. Figure 10(*a*) represents surface profiles corresponding to the two points marked by a diamond and a cross in figure 9(*a*). The solid profile in figure 10(*a*) corresponds to the point marked by a diamond in figure 9(*a*) and the dashed profile to the point marked by a cross. In figure 10(*b*) we have plotted corresponding profiles of the normalized axial normal viscous force Ψ_{xx}:

$$\Psi_{xx} = \frac{Fr^2}{Re}\frac{\partial_x F_{xx}}{\pi(1-d^2)}, \quad F_{xx} = 2\pi\int_d^1 \partial_x u r \,\mathrm{d}r. \tag{3.2a,b}$$

Here F_{xx} is the (dimensionless) axial viscous force acting on the cross-section of the liquid film. Its differential $\mathrm{d}F_{xx} = \partial_x F_{xx}\,\mathrm{d}x$ yields the resulting axial normal viscous force acting on a slice of liquid film. In (3.2) we have normalized $\mathrm{d}F_{xx}$ with the differential gravitational force to obtain Ψ_{xx}.

https://doi.org/10.1017/jfm.2020.267 Published online by Cambridge University Press

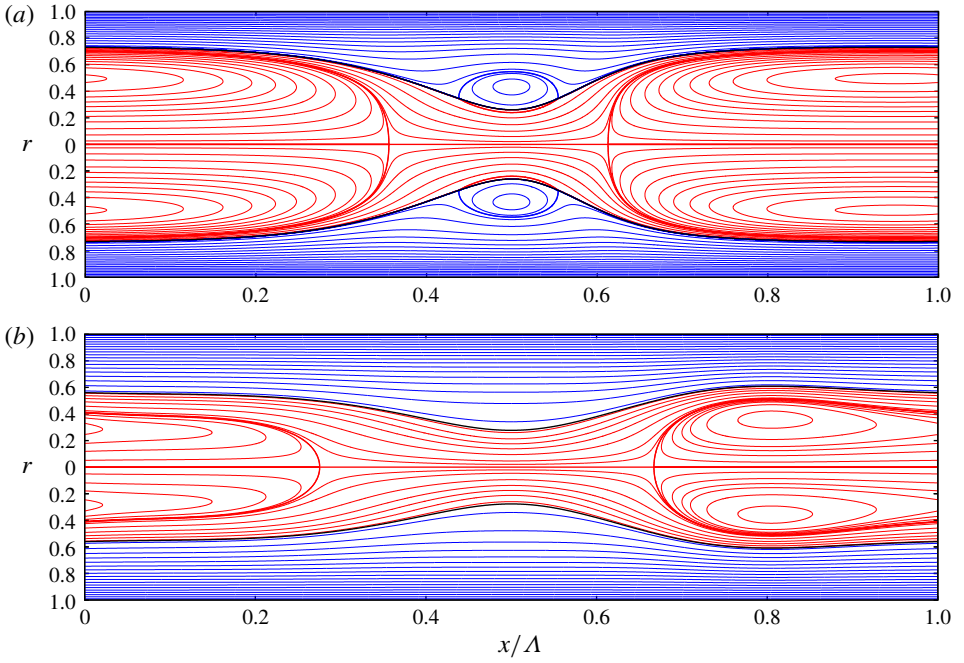


FIGURE 11. Streamlines in the wave-fixed reference frame for the marked limit points in figure 9(*c*). Blue lines correspond to liquid film and red lines to core gas flow. (*a*) Full model (2.5): filled circle in figure 9(*c*). The wave hump contains a vortex. (*b*) No axial viscous diffusion, i.e. $J_j = K_j = L_j = M_j = 0$ in (2.5): asterisk in figure 9(*c*). No vortex is predicted in the wave hump.

Grey and white areas underneath the solid curves in figures 10(*a*) and 10(*b*) identify regions where the axial normal viscous force is directed counter to ($\Psi_{xx} < 0$) or in the direction of ($\Psi_{xx} > 0$) gravity. Based on this, the arrows in figure 10(*a*) illustrate the resulting action of axial normal viscous stresses. This action tends to steepen the trailing front of the surface wave (where the residual film and the wave hump are pushed towards one another) and elongate the leading wave front (where residual film and wave hump are pulled away from one another). It counters the gravity-induced compression of the leading wave front and elongation of the trailing wave front and thus weakens the saturation mechanism discussed in § 3.3. The strength of the effect increases with increasing Reynolds number, as evidenced by comparing the two profiles in figure 10(*b*) and this explains why the solid and dot–dashed lines in figure 9(*a*) diverge with increasing *Re*.

Axial viscous diffusion also greatly affects the wave speed and the streamline pattern in the wave-fixed reference frame. In figure 9(*c*) we have replotted the continuation curves from figure 9(*a*) in terms of the fluid velocity at the wave crest $u(d_{min})$ normalized by the wave celerity c. When $u(d_{min}) > c$, a moving-frame vortex develops in the wave hump. Such waves are known as roll waves and the grey area in figure 9(*c*) delimits their existence. The limit point on the solid black line (filled circle) lies within this region, while the limit point on the dot–dashed line (asterisk) does not. This is illustrated by the corresponding streamline patterns in figure 11. Also, we see that the roll wave in figure 11(*a*) conveys with it a large gas bubble containing a toroidal vortex. This particular flow pattern results from the aerostatic pressure difference imposed here, i.e. $\Psi = 1$. Other gas flow scenarios will

https://doi.org/10.1017/jfm.2020.267 Published online by Cambridge University Press

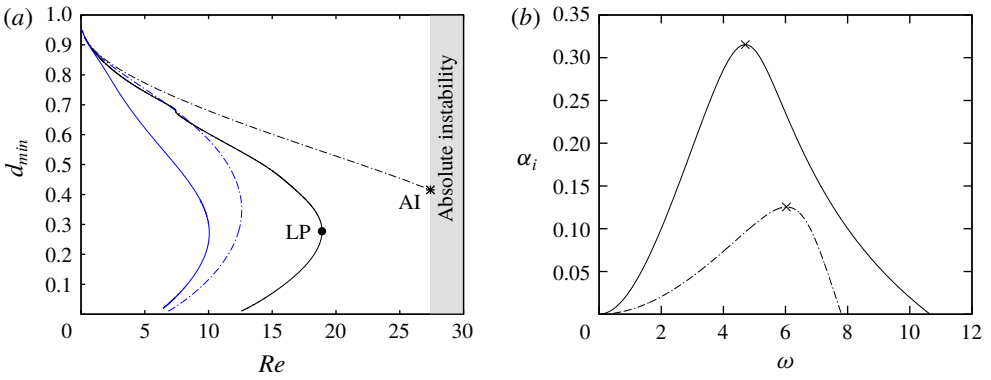


FIGURE 12. Precipitation of occlusion due to inertia. Case 4: low-viscosity silicone oil, $Bo = 0.993$. Solid lines, full model (2.5); dot–dashed lines, no inertia, $S_i = F_{ij} = G_{ij} = 0$ in (2.5) and (2.11). (*a*) Nonlinear travelling-wave solutions. Black lines with symbols: $f = f_{max}$. Blue lines without symbols: $\Lambda = 12.56$. (*b*) Dispersion curves of linear spatial growth rate α_i: $Re = 15.4$.

be discussed in § 3.6. Finally, we point out that the lower branches in figure 9 are the stable ones, and that only the full model, which accounts for axial viscous diffusion, predicts roll wave solutions on these branches.

3.5. *Role of inertia*

Inertia constitutes the growth mechanism of the Kapitza instability, which is responsible for the formation of surface waves on planar falling liquid films, and which becomes relevant in our current problem when Re is sufficiently large. This is the case for the low-viscosity silicone oil film (case 4). In figure 12 we have represented nonlinear travelling-wave solutions (figure 12*a*) and dispersion curves of the linear spatial growth rate α_i (figure 12*b*) for this case. Solid curves were obtained with our full model (2.5), and dashed curves by neglecting inertia, i.e. by setting $S_i = F_{ij} = G_{ij} = 0$ in (2.5) and (2.11).

In figure 12(*a*) we confront two types of travelling-wave continuations. On the blue lines without symbols, we have fixed the wavelength $\Lambda = 12.56$. In this case, the effect of inertia is purely nonlinear. We see that this effect significantly advances the limit point of the solid blue versus the dashed blue curve (by approximately 20 %). Inertia increases the cumulated strength of the destabilizing mechanisms (Plateau–Rayleigh and Kapitza instabilities) versus the stabilizing ones (capillarity and viscous dissipation). This limits the ability to saturate nonlinear travelling waves to smaller amplitudes, i.e. lower Re.

On the black lines with symbols, we have imposed $f = f_{max}$. Here, the effect of inertia is even stronger, as it additionally affects linear wave selection by determining the spatially most amplified wave frequency f_{max}. The linear dispersion curves in figure 12(*b*), where $Re = 15.4$, illustrate this effect. When inertia is taken into account (solid curve), $\omega_{max} = 2\pi f_{max}$ moves to smaller frequencies, which we have shown to precipitate the loss of travelling-wave solutions (figure 6*a* in § 3.2). Comparing the solid and dashed lines in figure 12(*a*), we see that inertia, similar to axial viscous diffusion, also dictates the nature of the occlusion mechanism. When it is taken into account, occlusion results from the loss of travelling-wave solutions at the limit point marking the upper occlusion bound Re_{max}. When it is neglected, occlusion occurs to absolute instability.

https://doi.org/10.1017/jfm.2020.267 Published online by Cambridge University Press

In addition to shifting Re_{max}, inertia also changes the nature of the occlusion bound in figure 12(*a*). If inertia is neglected, Re_{max} is dictated by absolute instability (AI, asterisk), otherwise, it is dictated by a nonlinear turning point (LP, filled circle). This qualitative change was also observed for the role of axial viscous diffusion in figure 9.

In the case of the classical Plateau–Rayleigh configuration, $Bo \to 0$, inertia only affects the dynamics of the film's evolution (Dietze & Ruyer-Quil 2015) but not the occlusion limit itself, because the latter is determined by a static equilibrium state (Everett & Haynes 1972).

3.6. *Role of core gas flow*

The gas in the core of the cylindrical tube can affect the liquid film falling down its inner wall in two ways: (i) through the normal and tangential interfacial viscous stresses τ_g^n and τ_g^t, which are scaled by Π_μ in (2.3); and (ii) through the interfacial gas pressure p_g, which is scaled by Π_ρ in (2.3). Up until now, we have assumed that the gas is subject to an aerostatic pressure difference, $\Psi = 1$, meaning that gravity is fully compensated in the gas. In that case, the gas flow is enslaved to the hydrodynamics of the liquid film and both the above effects are negligible. Nonetheless, this one-way coupling produces intricate flow structures in the gas, as has been suggested by figure 11(*a*) and will be discussed further based on figure 14(*a*).

Conversely, when the gas flows counter-currently at a Reynolds number Re_g of sufficient magnitude, it does affect the hydrodynamics of the liquid film, and this two-way coupling can significantly precipitate the upper occlusion bound Re_{max}. We show this in figure 13 based on case 4, which produces surface waves of sufficient amplitude to significantly constrict the core gas flow. Figure 13(*a*) represents travelling-wave solutions obtained by continuing Re at $f = f_{max}$ for different gas flow configurations. The solid black curve with a filled circle at the limit point corresponds to $\Psi = 1$, and the dashed curve to a counter-current gas flow with $Re_g = -17.27$. Comparing these two curves, we see that Re_{max} is significantly precipitated due to the counter-current gas flow (by roughly 25 %). We have checked that the gas flow does not meaningfully affect the most amplified frequency f_{max} and, thus, this precipitation is a nonlinear effect. The dashed curve also displays two qualitative changes. First, its lower branch turns forward at a second, lower, limit point, producing travelling-wave solutions of constant amplitude that exist far beyond Re_{max}. However, as we show in appendix C, these solutions are inaccessible in a real system. Thus, Re_{max} remains a representative occlusion bound also in the counter-current configuration. Second, solutions on the portion of the curve between the asterisk and the new limit point are stable, in contrast to those on the lower branch of the solid black curve, where $\Psi = 1$.

In figure 13(*b*) we illustrate the effect of the gas flow in another way. Here, Re_g is varied at a fixed liquid volume V_l, while maintaining $f = f_{max}$. Such a scenario may be relevant for mucus films in pulmonary capillaries. We see that travelling-wave solutions are lost when the magnitude of the counter-current gas flow $|Re_g|$ is increased beyond a limit point.

The effect of the gas flow on the occlusion bound Re_{max} observed in figure 13(*a*) results from the pressure coupling between gas and liquid and not from the gaseous interfacial viscous stresses. This is evidenced by the curves without symbols in figure 13(*a*), which pertain to different limits of the full-model continuation at $Re_g = -17.27$ (dashed curve). The blue solid curve without a symbol pertains to the limit $\Pi_\mu = 0$ and the dot–dashed curve to the limit $\Pi_\rho = 0$. Deactivating the gaseous viscous stresses ($\Pi_\mu = 0$, solid blue curve without symbols), changes Re_{max} very little. By contrast, deactivating the gas pressure effect ($\Pi_\rho = 0$, dot–dashed curve), almost

https://doi.org/10.1017/jfm.2020.267 Published online by Cambridge University Press

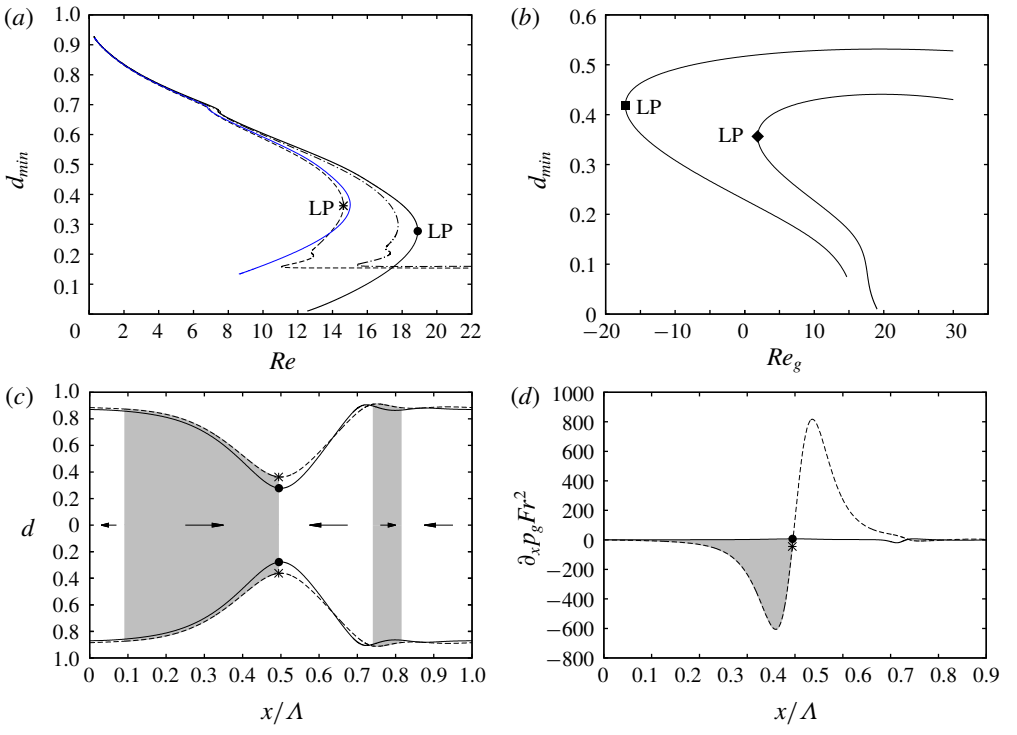


FIGURE 13. Precipitation of occlusion due to a counter-current gas flow. Case 4. (*a*) Travelling-wave continuation at $f = f_{max}$. Solid: aerostatic pressure drop, $\Psi = 1$. Dashed: counter-current gas flow, $Re_g = -17.27$. Solid blue line without symbol: $\Pi_\mu = 0$ in (2.5), $Re_g = -17.27$. Dot–dashed: $\Pi_\rho = 0$ in (2.5), $Re_g = -17.27$. (*b*) Continuation at $V_l =$ const. and $f = f_{max}$. Square, $V_l/\pi/R^3 = 2.435$; diamond, $V_l/\pi/R^3 = 2.770$. (*c*) Wave profiles corresponding to the asterisk and filled circle in panel (*a*). (*d*) Corresponding profiles of gas pressure gradient $\partial_x p_g$ according to (2.5*c*) (symbols mark position of wave maximum). Grey/white zones between the dashed profiles in panels (*c*,*d*) demarcate regions of negative/positive $\partial_x p_g$. Arrows in panel (*c*) indicate action of gas pressure gradient on the liquid film.

entirely negates the gas-induced precipitation of Re_{max} versus the aerostatic reference case (solid black curve with filled circle).

To elucidate the role of the gas pressure p_g, figures 13(*c*) and 13(*d*) represent wave profiles and corresponding profiles of the pressure gradient $\partial_x p_g$ for the two marked limit points in figure 13(*a*). Thereby, $\partial_x p_g$ is determined from (2.5*c*) and corresponds to the gas pressure gradient at the film surface $\partial_x p_g|_{r=d}$. We have dropped the accompanying subscripts for convenience. In figure 13(*d*), $\partial_x p_g$ is multiplied with Fr^2 in order to normalize the actual pressure gradient with the aerostatic one. Grey/white zones between the dashed lines in figures 13(*c*) and 13(*d*) distinguish regions of negative/positive $\partial_x p_g$ in the gas. In addition, figure 14 represents streamlines in the wave-fixed reference frame corresponding to the wave profiles in figure 13(*c*).

Focusing on the counter-current case, figure 14(*b*), we see that the wave hump produces a constriction through which the gas (flowing from right to left) must pass, similar to a de Laval nozzle that first accelerates and then decelerates the flow. This produces strong positive/negative pressure gradients to the right/left of the wave

https://doi.org/10.1017/jfm.2020.267 Published online by Cambridge University Press

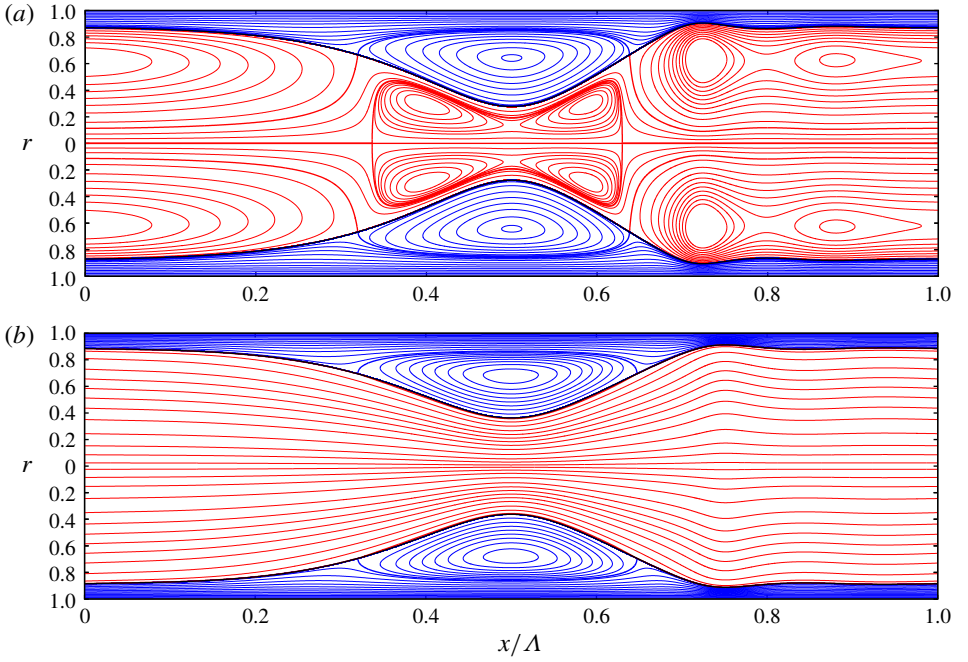


FIGURE 14. Streamlines in the wave-fixed reference frame corresponding to the marked limit points in figure 13(*a*). Within the film, liquid below the vortex flows from right to left. (*a*) Aerostatic gas pressure drop (filled circle in figure 13*a*): $\Psi = 1$, $Re = 18.9$, $\Lambda = 6.3$. (*b*) Counter-current gas flow (asterisk in figure 13*a*): $Re_g = -17.27$, $Re = 14.6$, $\Lambda = 5.7$. The gas, flowing from right to left, is constricted by the wave hump, similar to a de Laval nozzle.

maximum (see dashed line in figure 13*d*) and these tend to push the liquid within the film towards the wave hump (arrows in figure 13*c*). This mechanism tends to increase the wave amplitude for a given Re and thus to advance the occlusion bound Re_{max}. It requires a sufficiently strong relative motion between the travelling wave and the gas. This does not necessarily require an upward gas flow. Indeed, the diamond-marked curve in figure 13(*b*) shows that occlusion may be brought about even when the gas is co-current, at least if $|Re_g|$ is sufficiently small.

In the aerostatic case, $\Psi = 1$, axial pressure variations in the core are very weak (solid line in figure 13*d*) and the gas has no incidence on the occlusion limit. *Vice versa*, the flow structure in the gas is strongly affected by the liquid film. We see this in figure 14(*a*), which pertains to case 4 (low-viscosity silicone oil), and also in figure 11(*a*), which pertains to case 1 (high-viscosity silicone oil). In both examples, the gas flow is enslaved to the liquid surface flow (through (2.3*a*)), which exhibits interfacial stagnation points around the wave hump, as a result of the moving-frame vortex in the liquid film. Due to this, the gas flow is divided into an intricate system of vortices. The constellation of these vortices is dictated by the strength of the liquid vortex in the wave hump.

3.7. *Occlusion scenarios in a spatially evolving film*

In § 3.2 we introduced the conservative occlusion bounds Re_0 and Re_{max} based on the limit of travelling-wave solutions and delimited three regimes for a naturally evolving

https://doi.org/10.1017/jfm.2020.267 Published online by Cambridge University Press

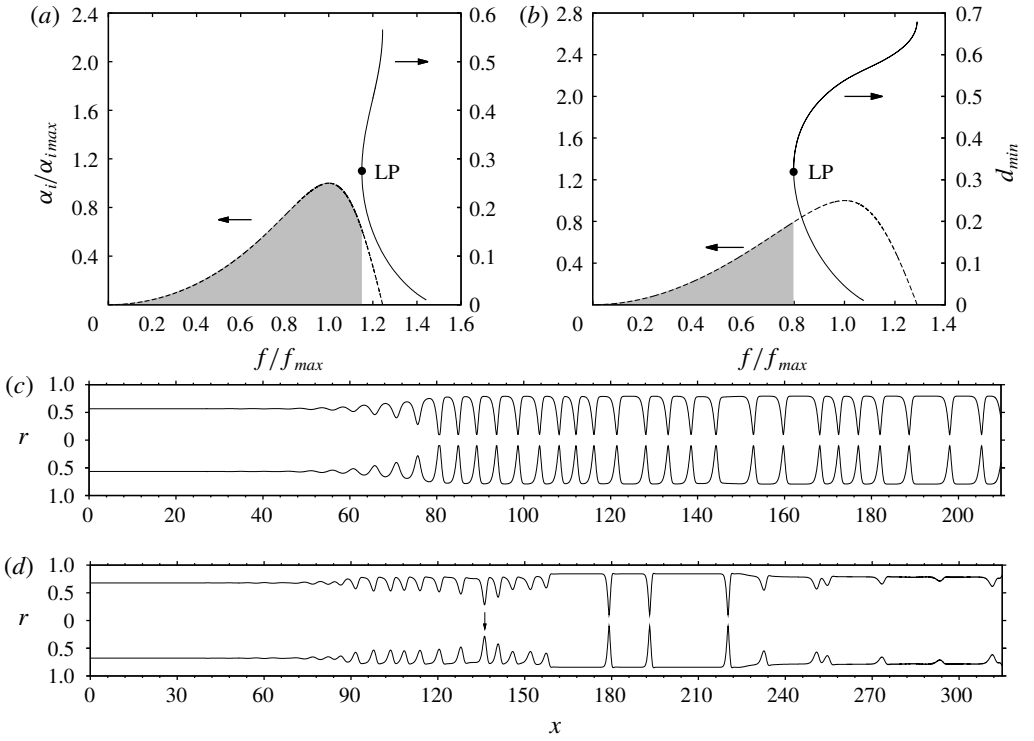


FIGURE 15. Different routes to occlusion in a spatially evolving film. Computations of experimental runs 20 (*a*,*c*) and 13 (*b*,*d*) in Dao & Balakotaiah (2000). (*a*,*b*) Travelling wave solutions (right abscissae) at $Re = \text{const.}$, and dispersion curves of the linear spatial growth rate α_i (left abscissae). Grey zones distinguish linear waves that have no saturated travelling state. (*c*,*d*) Spatio-temporal computations on an $L^\star = 1$ m domain with inlet noise (2.6*b*). (*a*,*c*) Experimental run 20: case 2 in table 1, $Re = 0.0497$ (regime of certain occlusion, scenario I). (*b*,*d*) Experimental run 13: case 3 in table 1, $Re = 0.258$ (regime of conditional occlusion, scenario II). The arrow in panel (*d*) marks a coalescence event triggering occlusion.

wavy falling liquid film: (i) impossible occlusion, when $Re < Re_0$; (ii) conditional occlusion, when $Re_0 < Re < Re_{max}$; and (iii) certain occlusion, when $Re > Re_{max}$. We now demonstrate these regimes based on spatio-temporal computations with our model (2.5), where we have mimicked naturally evolving waves through the noisy inlet condition (2.6*b*), using $\epsilon_2 = 10^{-5}$. For the gas, we have imposed $\Psi = 1$.

We start by reproducing two of the occlusion experiments of Dao & Balakotaiah (2000), i.e. their experimental runs 20 and 13 which identified the experimental occlusion point at $Re = 0.0497$ and $Re = 0.258$, respectively. These two runs correspond to our cases 2 and 3 in table 1, for which we have determined the lower/upper occlusion bounds in § 3.2 as $Re_0 = 0.012/Re_{max} = 0.038$ (figure 5*c*) and $Re_0 = 0.075/Re_{max} = 0.39$ (figure 5*d*), respectively. Based on this, experimental run 20 (our case 2) lies in the region of certain occlusion and experimental run 13 (our case 3) in the region of conditional occlusion. This is confirmed by figure 15(*a*) and 15(*b*), which represent travelling-wave solutions continued in terms of the wave frequency f (right abscissae) and dispersion curves of the linear growth rate α_i (left abscissae) for these two runs.

https://doi.org/10.1017/jfm.2020.267 Published online by Cambridge University Press

The experiments of Dao & Balakotaiah (2000) were performed in a long vertical tube equipped with a conductance probe that allowed us to detect occlusion locally. However, no information on the film's surface dynamics upstream of this point was available. We provide this missing information in figures 15(*c*) and 15(*d*), which represent snapshots of our spatio-temporal computations reproducing experimental runs 20 and 13. These computations were performed on an $L^\star = 1$ m domain. We see that the two cases reach occlusion by two very different routes, as a result of distinct wave dynamics.

For experimental run 20 (our case 2), most of the dispersion curve in figure 15(*a*) (grey area) lies beyond the limit point of travelling-wave solutions ($f_{max} < f_{LP}$). Thus, the most amplified surface waves emerging from the linear regime do not possess any saturated travelling state and inevitably cause occlusion by extending their growth into the nonlinear regime (figure 15*c*). This is occlusion scenario I, which we had already observed for case 1 (high-viscosity silicone oil) in figure 4. Supplementary movie M2 shows the computation from figure 15(*c*) in action. We remind the reader that the unphysical plug reopening observed therein (and in supplementary movie M3) is due to the crude numerical core radius limitation introduced in § 2.1. First results in appendix E suggest that this artefact is negated by our improved WRIBL model (figure 22).

By contrast, for experimental run 13 (our case 3), the most amplified linear waves lie well within the range of travelling-wave solutions ($f_{max} > f_{LP}$ in figure 15*b*). Occlusion must therefore occur through a different route, as evidenced by the wave profile in figure 15(*d*). In the first part of the tube ($x \leqslant 130$), a quite regular train of saturated-amplitude travelling waves develops. These result from linear wave selection and their minimal core radius d_{min} is far from reaching the tube axis. However, individual waves within the wave train are quite narrowly spaced and thus prone to the secondary subharmonic/sideband instabilities typically associated with single-humped waves in planar falling liquid films (Chang, Demekhin & Kopelevich 1993; Liu & Gollub 1993). These instabilities result from wave interactions triggered by residual noise and lead to wave coalescence, which is the first step in the so-called wave coarsening dynamics identified by Chang *et al.* (1996*b*). This cascaded dynamics produces ever longer, more dangerous, waves by successive coalescence/absorption events and, thus, represents an inherent route towards occlusion. The arrow in figure 15(*d*) highlights one such coalescence event, which produces a wave of greater amplitude that will occlude the tube and subsequently absorb several smaller waves downstream.

This is occlusion scenario II, which is intermittent because the initiating wave coalescence is occasional, in contrast to scenario I (figure 15*c*), where (almost) every wave grows to occlude the tube. Due to this intermittence, gas bubbles resulting from successive occlusion events are much more unevenly distributed. Supplementary movie M3 shows the computation from figure 15(*d*) in action.

We now focus on case 3 and compute the spatio-temporal wave evolution for values of Re below the experimental occlusion threshold $Re = 0.258$ determined in run 13 of Dao & Balakotaiah (2000). This experimental threshold lies well within the region of conditional occlusion, which is bounded by $Re_0 = 0.075$ and $Re_{max} = 0.393$ (figure 5*d*).

Figure 16(*a*) represents a spatio-temporal computation at a lower Reynolds number $Re = 0.14 > Re_0$, which still lies in the conditional occlusion regime. This computation was performed on a domain of $L^\star = 2$ m in length, i.e. twice longer than the one in figure 15(*d*). We see that occlusion still occurs, through scenario II, but that the occlusion point has shifted greatly downstream with respect to figure 15(*d*). The reason for this is that the frequency/wavelength of the limiting travelling waves

https://doi.org/10.1017/jfm.2020.267 Published online by Cambridge University Press

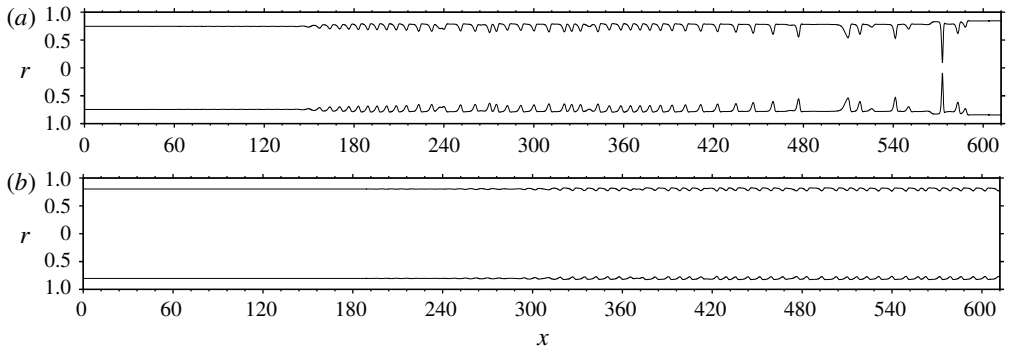


FIGURE 16. Computations of case 3 ($Re_0 = 0.075$, $Re_{max} = 0.39$; figure 5*b*) at lower Re, showing a downstream displacement of the occlusion point with respect to figure 15(*d*). Spatio-temporal computations on an $L^\star = 2$ m domain with inlet noise (2.6*b*). (*a*) $Re = 0.14$: regime of conditional occlusion. Occlusion (through scenario II) occurs much further downstream than in figure 15(*d*). (*b*) $Re = 0.07 < Re_0$: regime of impossible occlusion. Surface waves are extremely small.

greatly decreases/increases with decreasing Re (see figure 5*d*) and, thus, much more space is needed for these to develop from the coarsening dynamics. The downstream shift in the occlusion point explains why Dao & Balakotaiah (2000), who checked for occlusion in a fixed region, found an experimental threshold for Re that is greater than the lower conservative bound Re_0. It also clearly shows that occlusion in the conditional regime (through scenario II) depends on whether the tube is sufficiently long to accommodate formation of those waves that are able to cause occlusion. As these waves may be much longer than those emerging from linear selection, occlusion may require unrealistically long tube lengths, depending on Re. Supplementary movie M4 shows the computation from figure 16(*a*) in action.

Conversely, occlusion in an infinitely long tube will eventually always occur if Re lies within the conditional regime, at least for a naturally evolving film. This is due to the nature of the coarsening dynamics, which halts only after truly solitary waves have formed. Thus, to avoid occlusion in an infinitely long tube, Re must be decreased below the lower conservative bound Re_0, where even solitary waves are too small to cause occlusion. In figure 16(*b*) we show a computation under such conditions, i.e. $Re = 0.07 < Re_0$. Although occlusion is indeed avoided, surface waves are extremely small in amplitude, which thwarts their beneficial effect on heat and mass transfer (Yoshimura, Nosoko & Nagata 1996; Albert, Marschall & Bothe 2013). This underlines the conservative nature of the lower occlusion bound Re_0. We will show in the next section that there is another way to prevent occlusion, namely through coherent inlet forcing in the conditional occlusion regime, which allows maintaining surface waves of significant amplitude.

Finally, in figure 17 we show snapshots of three representative spatio-temporal computations for case 4 (low-viscosity silicone oil), where inertia, which drives the Kapitza instability, is relevant. Figures 17(*a*), 17(*b*) and 17(*c*) correspond to the regimes of certain, conditional and impossible occlusion, respectively. These display the same main features observed for the high-viscosity liquids (figures 15*c*, 16*a* and 16*b*), only that the length scales of the occlusion processes are much shorter.

https://doi.org/10.1017/jfm.2020.267 Published online by Cambridge University Press

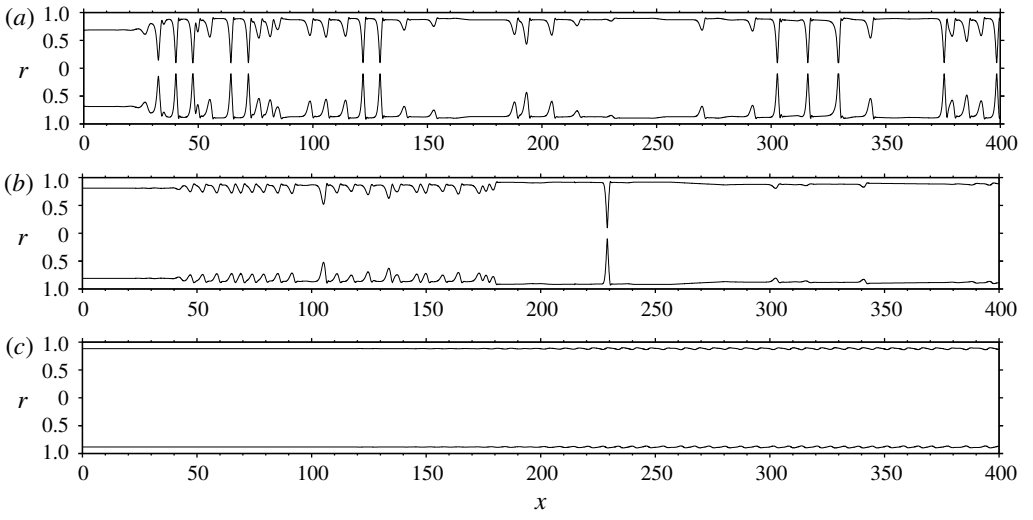


FIGURE 17. Different occlusion scenarios for case 4 ($Re_0 = 1.5$, $Re_{max} = 18.9$; figure 6*b*). Spatio-temporal computations on an $L^\star = 1$ m domain with inlet noise (2.6*b*). (*a*) $Re = 19 > Re_{max}$: regime of certain occlusion (scenario I). (*b*) $Re = 5$: regime of conditional occlusion (scenario II). (*c*) $Re = 1.25 < Re_0$: regime of impossible occlusion. Surface waves are extremely small.

3.8. *Coherent inlet forcing to prevent occlusion*

For $Re > Re_0$, travelling-wave solutions are bounded by a limiting frequency f_{LP}, below which they cannot exist and occlusion is inevitable (see figures 5*d* and 6*b*). Conversely, by increasing f above f_{LP}, travelling-wave solutions are recovered and occlusion can be avoided. We thus test the idea of forcing high-frequency waves through coherent inlet forcing in a spatially evolving falling liquid film, in order to prevent occlusion without having to reduce Re below the conservative bound Re_0, where surface waves all but disappear (see figures 16*b* and 17*c*).

This idea works only in the conditional occlusion regime, $Re_0 < Re < Re_{max}$. Indeed, in the regime of certain occlusion, $Re > Re_{max}$, where $f_{LP} > f_{max}$, one would have to force waves of frequency $f > f_{max}$. Such short waves are very sensitive to the secondary instabilities causing wave coalescence in closely packed wave trains (Liu & Gollub 1993), and rapidly loose the signature of the inlet forcing. By contrast, in the conditional occlusion regime, f_{LP} can be low enough (the lower Re, the lower f_{LP}) to allow forcing a wave train that is not subject to secondary instability.

We demonstrate this by running the spatio-temporal computations in figures 16(*a*) (case 3) and 17(*b*) (case 4) again with additional coherent inlet forcing. For this, we activate the monochromatic perturbation in (2.6*b*) with a relative amplitude $\epsilon_1 = 0.1$. Meanwhile, the inlet noise remains active and its level unchanged $\epsilon_2 = 10^{-5}$. We stress that ϵ_2 in (2.6*b*) is the scale factor of a Fourier series with a 1000 terms. Thus, the actual noise amplitude is much greater than suggested by the value of ϵ_2. It is about 10 % of ϵ_1 for the runs presented here. The forcing frequency f is chosen greater than the limit value f_{LP} of travelling-wave solutions, as obtained from figures 5(*d*) (case 3, $Re = 0.14$, $f_{LP} = 0.41 f_{max}$) and 6(*b*) (case 4, $Re = 5$, $f_{LP} = 0.35 f_{max}$), respectively.

In figures 18(*a*) and 18(*b*) we show the results of our spatio-temporal computations with additional coherent inlet forcing and are to be compared directly to figures 16(*a*) and 17(*b*), where the wave dynamics are purely noise-driven. We see that the

https://doi.org/10.1017/jfm.2020.267 Published online by Cambridge University Press

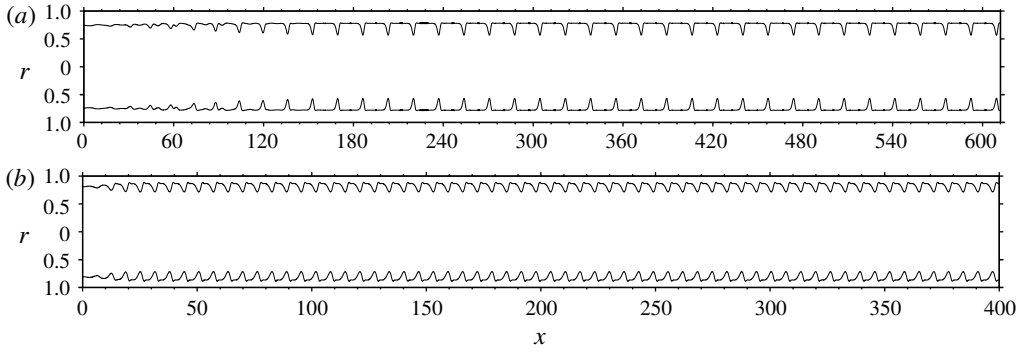


FIGURE 18. Preventing occlusion in the conditional occlusion regime, $Re_0 < Re < Re_{max}$, through coherent inlet forcing. Spatio-temporal simulations from figures 16(*a*) and 17(*b*) with additional coherent inlet forcing of frequency f and amplitude $\epsilon_1 = 0.1$ (2.6*b*). All other parameters, including the noise level ϵ_2, remain unchanged. (*a*) Case 3 ($Re_0 = 0.075$, $Re_{max} = 0.393$; figure 5*d*): $Re = 0.14$, $f = 0.5 f_{max} = 0.525$. (*b*) Case 4 ($Re_0 = 1.5$, $Re_{max} = 18.9$; figure 6*b*): $Re = 5$, $f = 0.5 f_{max} = 1.27$. Coherent inlet forcing produces a regular train of saturated-amplitude travelling waves, allowing us to prevent occlusion versus the natural evolution in figures 16(*a*) and 17(*b*).

additional coherent inlet forcing produces a regular train of saturated-amplitude travelling waves that do not occlude the tube. This wave train is maintained over the entire length of the domain and, thus, robust with respect to secondary instability. In contrast to figures 16(*b*) and 17(*c*), where occlusion was avoided by reducing Re below the lower conservative bound Re_0, the falling films in figures 18(*a*) and 18(*b*) display quite substantial surface waves, expected to be much more beneficial for inter-phase heat and mass transfer.

4. Conclusion

We have studied numerically the occlusion of a narrow vertical cylindrical tube by an axisymmetric wavy falling liquid film in contact with a laminar core gas flow. We have focused on conditions where the effect of gravity is at least comparable to that of capillarity, i.e. $Bo \geqslant 1$, and the gas Reynolds number Re_g is quite low. In that limit, occlusion is caused by spatially growing waves and not by absolute linear instability. These waves are generated by a combination of the Plateau–Rayleigh instability, gravity-driven advection and the Kapitza instability.

Using the low-dimensional model introduced in Dietze & Ruyer-Quil (2015), which had been applied only to gravity-free films, we have performed spatio-temporal computations of spatially evolving falling films and computed travelling-wave solutions through numerical continuation. Our model extends upon the earlier works of Trifonov (1992), Camassa *et al.* (2014, 2017), Zhou *et al.* (2016), Liu & Ding (2017) and Ding *et al.* (2019) by accounting for axial viscous diffusion and inertia. These effects are needed to accurately predict occlusion for the real liquids studied here (cases 1–4 in table 1). We have validated our model computations with DNS (appendix A and figure 5*d*).

Travelling-wave solutions are lost when the liquid Reynolds number Re is increased beyond a limit point, low-frequency/long waves being more dangerous (smaller Re_{LP}) than high-frequency/short waves (greater Re_{LP}). By numerically reproducing the

https://doi.org/10.1017/jfm.2020.267 Published online by Cambridge University Press

occlusion experiments of Camassa *et al.* (2014), we have proved that surface waves causing occlusion systematically lie beyond this limit of travelling-wave solutions, thus validating the conjecture formulated by these authors.

Depending on how occluding waves emerge in a spatially evolving film, either directly from linear wave selection (scenario I) or subsequent secondary instability and wave coarsening (scenario II), we have distinguished two possible occlusion scenarios. By reproducing several occlusion experiments with our own spatio-temporal computations, we have shown that occlusion scenario I (figures 4*a* and 15*c*, movie M2) applies to the experiments of Camassa *et al.* (2014) and run 20 in Dao & Balakotaiah (2000), while scenario II (figure 15*d*, movie M3) applies to run 13 in Dao & Balakotaiah (2000).

We have delimited scenarios I and II based on an upper conservative occlusion bound Re_{max}, which corresponds to the limit point of travelling-wave solutions at the spatially most amplified frequency f_{max} of linear waves. And, a lower conservative bound Re_0, below which travelling-wave solutions always exist, no matter how great the wavelength (Ding *et al.* 2019). Determining Re_{max} requires computing f_{max} and, thus, we have simultaneously solved the linear stability problem in our numerical continuations. This had not been attempted in previous studies (Camassa *et al.* 2014; Ding *et al.* 2019).

Based on the upper and lower conservative bounds Re_{max} and Re_0, as well as spatio-temporal computations, we have delimited three possible regimes for a naturally evolving wavy film: (i) certain occlusion: $Re > Re_{max}$. The most amplified surface waves, which typically emerge in an experiment, do not possess travelling states. Occlusion is inevitable and occurs through scenario I; (ii) conditional occlusion: $Re_0 < Re < Re_{max}$. Occlusion is theoretically possible through scenario II (for long enough waves), but does not necessarily occur in a real system. This depends on whether the coarsening dynamics can produce sufficiently long waves and whether the tube is long enough to accommodate this (figures 15*d* and 16*a*, movies M3 and M4); (iii) impossible occlusion: $Re < Re_0$. All possible surface waves, no matter how long, are safe.

We have shown that occlusion can be actively prevented in the regime of conditional occlusion ($Re_0 < Re < Re_{max}$) by forcing waves of sufficiently high frequency through coherent inlet forcing (figures 18*a* and 18*b*). This allows us to maintain surface waves of non-negligible amplitude, in contrast to the regime of impossible occlusion ($Re < Re_0$) where waves are almost invisible (figures 16*b* and 17*c*). Given the well documented positive effect of surface waves on inter-phase heat/mass transfer (Yoshimura *et al.* 1996), coherent inlet forcing is an attractive route to enhance transfer while avoiding occlusion.

We have computed the lower and upper conservative bounds Re_0 and Re_{max} for the four working liquids considered here (figures 5 and 6). Furthermore, we have quantified how key parameters (Bo and Re_g) as well as several physical effects (axial viscous diffusion and inertia) affect the upper conservative bound Re_{max}, which delimits the regimes of certain and conditional occlusion. We have found that gravity greatly delays this bound, significantly increasing Re_{max} as the Bond number Bo is increased (see figure 8*a*). Unless Bo is very large, the height of travelling waves at $Re = Re_{max}$ is far from reaching the tube radius. In contrast to what Dao & Balakotaiah (2000) conjectured, such solutions are thus lost abruptly and not due to the wave height reaching the tube radius continuously.

We have found that a laminar counter-current gas flow can significantly precipitate occlusion for low-viscosity liquids (low-viscosity silicone oil, case 4), where the effect

https://doi.org/10.1017/jfm.2020.267 Published online by Cambridge University Press

of the gas pressure becomes relevant in the liquid force balance. At the strongest gas flow studied ($Re_g = -17$), we have observed a 25 % reduction of Re_{max} (figure 13*a*) versus a situation where the gas is quiescent. We have found that the gas affects the liquid film mainly through inter-phase pressure coupling. Surface waves locally constrict the gas flow, which is accelerated and then decelerated as it passes through (figure 14*b*). This produces a pressure minimum above the wave crest that sucks liquid towards the wave, tending to increase its amplitude and, thus, the danger of occlusion.

For high-viscosity liquids (high-viscosity silicone oil and aqueous glycerol solution, cases 1 and 3), axial viscous diffusion greatly precipitates occlusion, i.e. greatly reduces Re_{max} (by 74 % in figure 9*a*). This may be relevant for mucus films within the first five generations of the human respiratory network, where the capillary radius is large enough for gravity to be relevant (King & Macklem 1977; Lewis *et al.* 2005; Grotberg 2011).

For low-viscosity liquids (low-viscosity silicone oil, case 4), we have observed that Re_{max} becomes large enough for inertia to be relevant ($Re_{max} = 18.9$ in figure 6*a*). This activates the Kapitza instability, which tends to increase the amplitude of travelling-waves, increasing the danger of occlusion. We have found that inertia significantly precipitates occlusion, decreasing Re_{max} versus an inertialess computation (by 20 % in figure 12*a*). This may be relevant for falling film micro-reactors (Seebauer *et al.* 2012).

Finally, we have found that neglecting axial viscous diffusion (high-viscosity liquids, figure 9*a*) or inertia (low-viscosity liquids, figure 12*a*) can change the nature of the occlusion mechanism, from being dictated by the loss of travelling-wave solutions to being dictated by absolute linear instability.

Our transient computations on long open domains have been performed with a crude numerical core radius limitation allowing us to continue these past occlusion events. Although this technique does not affect the wave dynamics leading up to occlusion, which is the focus of our current study, it does not represent the physics of liquid plugs to satisfaction. To remedy this, we have introduced an improved version of our WRIBL model (2.5) by augmenting it with an additional force term (E 1), allowing us to form stable travelling pseudo-plugs (figure 22). First results reported in appendix E suggest that this improved model negates the main artefact of the numerical core radius limitation, i.e. the reopening of liquid plugs. Confronting our improved model with full-fledged plug models (Suresh & Grotberg 2005; Ubal *et al.* 2008) is an enticing prospect for future work.

Acknowledgement

This work was supported by the ANR wavyFILM project, grant ANR-15-CE06-0016-01 of the French Agence Nationale de la Recherche.

Declaration of interests

The authors report no conflict of interest.

Supplementary movies

Supplementary movies are available at https://doi.org/10.1017/jfm.2020.267.

Appendix A. Validation of the WRIBL model based on transient DNS

Figure 19 represents comparisons between our WRIBL model (2.5) and DNS using the solver Gerris (Popinet 2009). All computations were performed for case 4 (low-viscosity silicone oil), which is the most challenging. The solid and dashed curves in

https://doi.org/10.1017/jfm.2020.267 Published online by Cambridge University Press

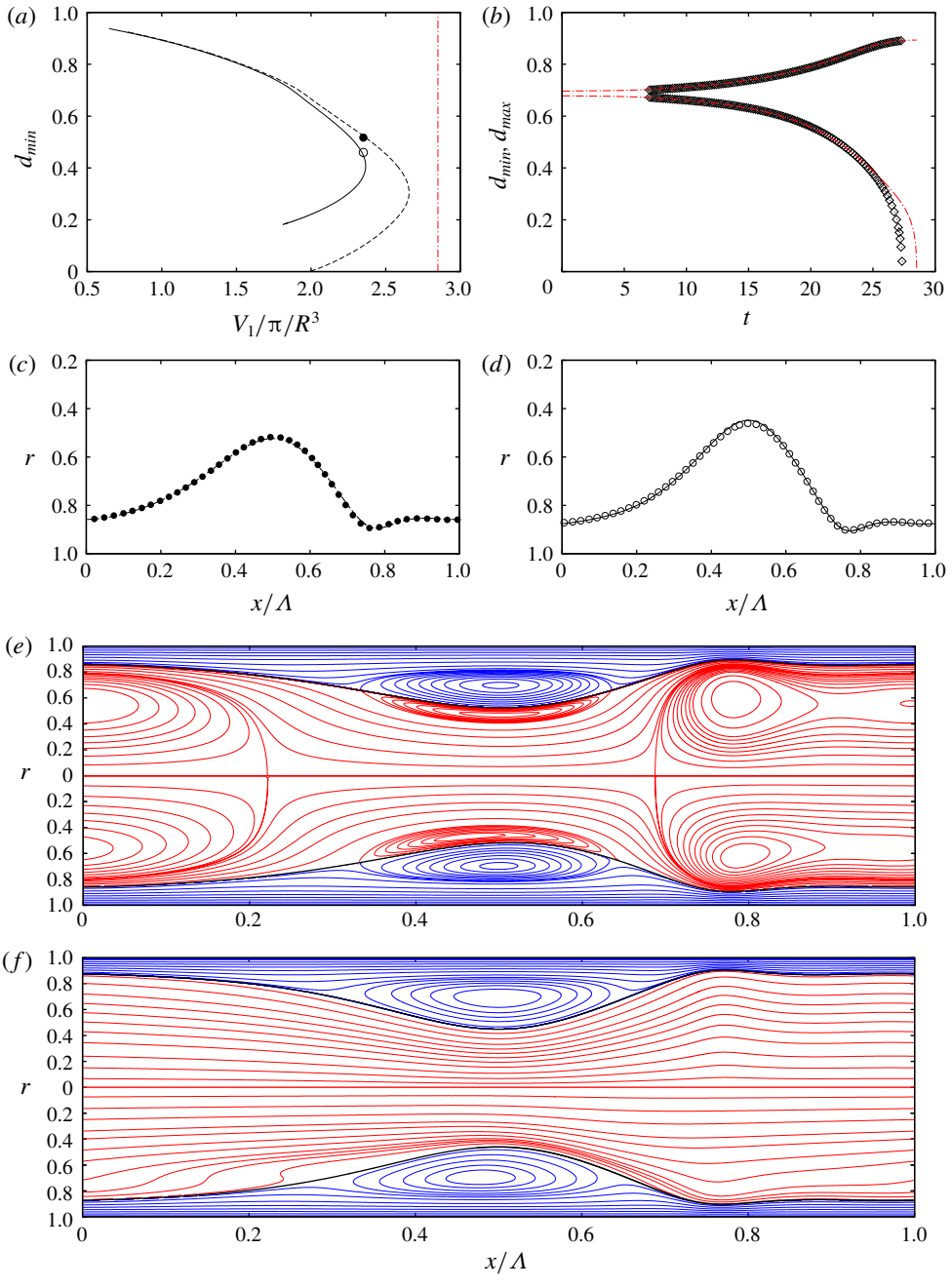


FIGURE 19. Validation of our WRIBL model (2.5) with DNS using the solver Gerris (Popinet 2009). Case 4 in table 1: low-viscosity silicone oil, $R^\star = 1.5$ mm. (*a*) Travelling-wave solutions at fixed $\Lambda = 5.4$. Dashed line (WRIBL) and filled circle (DNS, $V_l/\pi/R^3 = 2.35$): aerostatic pressure drop, $\Psi = 1$. Solid line (WRIBL) and open circle (DNS, $V_l/\pi/R^3 = 2.35$): $Re_g = -17.3$. (*b*) Transient periodic computations with DNS solver (diamonds) and WRIBL model (dot–dashed line): $\Lambda = 5.4$, $\Psi = 1$, $V_l/\pi/R^3 = 2.85$ (vertical line in panel *a*). (*c*,*d*) Profiles of travelling waves from panel (*a*) for $V_l/\pi/R^3 = 2.35$. Filled/open circles: DNS. Dashed/solid lines: WRIBL. (*e*,*f*) Streamlines in the wave-fixed reference frame for solutions in panels (*c*) and (*d*). Top half: WRIBL. Bottom half: DNS.

https://doi.org/10.1017/jfm.2020.267 Published online by Cambridge University Press

figure 19(*a*) represent travelling-wave solutions obtained with our model by continuing the liquid volume V_l at fixed wavelength $\Lambda = 5.4$ for two different gas flow situations. The dashed line corresponds to an aerostatic gas pressure drop $\Psi = 1$, and the solid line to a counter-current gas flow at $Re_g = -17.3$. We compare these data with two punctual DNS at $V_l/\pi/R^3 = 2.35$, which are marked by a filled ($\Psi = 1$) and open circle ($Re_g = -17.3$), respectively. Figures 19(*c*) and 19(*d*) represent the corresponding surface profiles at this point, as obtained from DNS (symbols) and our model (lines). Figures 19(*e*) and 19(*f*) represent corresponding streamline patterns in the wave-fixed reference frame. The top half of these graphs represents our model computations and the bottom half our DNS.

Finally, in figure 19(*b*) we compare time traces of the minimal and maximal core radius d_{min} and d_{max} obtained from transient periodic computations with our model (dot-dashed line) and the DNS solver (diamonds) for $\Lambda = 5.4$, $\Psi = 1$ and $V_l/\pi/R^3 = 2.85$ (vertical line in figure 19*a*), which lies beyond the limit point of travelling-wave solutions in figure 19(*a*). Agreement between the two data sets in figure 19(*b*) is good and both computations produce an occlusion of the tube by the liquid film, as evidenced by the divergence of the minimal core radius d_{min}. This confirms that occlusion occurs beyond the limit of travelling-wave solutions and that our model is able to capture the associated dynamics.

Appendix B. Numerical procedure for travelling-wave DNS

The DNS results in figure 5(*d*) were obtained by solving the full governing equations (2.1)–(2.3) in the limit $\Pi_\mu = \Pi_\rho = 0$ with a pseudo-spectral approach. For this, the liquid velocity and pressure fields are projected on modified Chebyshev polynomials

$$u_l(x, r, t) = \sum_{i=1}^{n} a_i(x, t)\phi_i(X), \quad p_l(x, r, t) = \sum_{i=0}^{n-1} b_i(x, t)\psi_i(X), \tag{B 1a,b}$$

where $X = 2(R - r)/(R - d) - 1$. The radial velocity v_l is obtained by integrating (2.1*b*), i.e. $v_l = -(1/r)\int_R^r \partial_x u_l r \,\mathrm{d}r$. The functions $\phi_i(X)$ and $\psi_i(X)$ are linear combinations of Chebyshev polynomials of the first kind T_i, i.e.

$$\left.\begin{gathered} \phi_1 = 1 + X, \quad \psi_0 = 1, \quad \psi_1 = X - 1, \\ \phi_{2i} = \psi_{2i} = T_{2i}(X) - 1, \quad \phi_{2i+1} = \psi_{2i+1} = T_{2i+1}(X) - X \quad \forall\, i \geqslant 1, \end{gathered}\right\} \tag{B 2}$$

so that $\phi_i(X = -1) = 0$ and, thus, the boundary conditions (2.2) are fulfilled.

Writing the Navier–Stokes equations (2.1*a*) on the Gauss–Lobato points $X_i = -\cos(\pi i/n)$ for $i \geqslant 1$, and introducing the wave-fixed coordinate $\xi = x - ct$, yields $2(n - 1)$ relations:

$$\left.\begin{gathered} \sum_{j=0}^{n-1} \psi_j(X_i) D_\xi b_j = \mathcal{F}_i(b_i, a_i, D_\xi a_i, D_{\xi\xi} a_i, h, D_\xi h, D_{\xi\xi} h), \\ \frac{1}{4Re}\frac{h}{r}\sum_{j=1}^{n}[\mathcal{C}_j(X_i) + I_j(X_i)] D_{\xi\xi\xi} a_i = \mathcal{G}_i(b_i, a_i, D_\xi a_i, D_{\xi\xi} a_i, h, D_\xi h, D_{\xi\xi} h). \end{gathered}\right\} \tag{B 3}$$

https://doi.org/10.1017/jfm.2020.267 Published online by Cambridge University Press

Here $D_\xi = \mathrm{d}/\mathrm{d}\xi$, $\mathcal{C}_j = \int_{-1}^{X} X(\phi_j)'\,\mathrm{d}X$ and $I_j = \int_{-1}^{X} \phi_j\,\mathrm{d}X$. Furthermore, we have

$$\left.\begin{array}{c} \tau_l^t = \eta D_{\xi\xi\xi} a_1, \\ \tau_l^n + Re p_l - Re\, We^{-1}\kappa = \eta D_\xi b_0, \\ q_l + c\pi d^2 = \eta D_{\xi\xi\xi} h, \end{array}\right\} \tag{B 4}$$

and, thus, the free-surface dynamic conditions (2.3*b*)–(2.3*c*) and the integral continuity equation (2.5*a*) are recovered in the limit $\eta \to 0$. We finally obtain the linear equation system

$$\boldsymbol{A}\frac{\mathrm{d}\boldsymbol{U}}{\mathrm{d}\xi} = \boldsymbol{B}(\boldsymbol{U};\,\eta) \tag{B 5}$$

for the unknowns $\boldsymbol{U} = (h,\, D_\xi h,\, D_{\xi\xi} h,\, a_i,\, D_\xi a_i,\, D_{\xi\xi} a_i,\, b_{i-1})\ \forall\ 1 \leqslant i \leqslant n$. Inverting (B 5) leads to an autonomous dynamical system of dimension $4n+3$. This dynamical system was solved with the continuation software AUTO07P (Doedel 2008), using a predictor–corrector method (Kalliadasis *et al.* 2012). Our computations were performed with $\eta = 10^{-6}$ and $n = 20$, which we have determined based on convergence tests.

Appendix C. Travelling waves on the lower branch in figure 13(*a*)

We discuss further the travelling-wave solutions on the lowest branch of the dashed curve in figure 13(*a*), which extends beyond the limit point $Re = Re_{max}$, as the result of interfacial viscous stresses exerted by the gas. Figure 20(*a*) replots that curve (dashed line) and the corresponding curve for the aerostatic configuration (solid line) in terms of the pressure gradient $\Psi = \Delta p_g Fr^2$. The filled circles therein correspond to the limit points in figure 13(*a*). The segment of the dashed curve that we are interested in lies above the asterisk, and we have checked the stability of solutions thereon, using transient periodic computations with imposed Ψ (we recall that the red portion of the curve, between the circle and asterisk, is stable). As Re is increased on this curve segment, solutions go from being stable to being subject to an oscillatory instability, similar to that found in planar channels (Lavalle *et al.* 2020). In both situations, our transient periodic computations do not produce occlusion.

However, these states are inaccessible in a real system, where Re is fixed and the counter-current gas flow is imposed through Ψ. The arrow in figure 20(*a*) indicates how Ψ would need to be varied to attain the desired states, starting from the aerostatic situation (marked by a cross). Besides that this would require a two hundred fold increase of Ψ, it turns out that there is no continuation path (at $Re = \text{const.}$) from the solid curve, where $\Psi = 1$, to the dashed curve, where $Re_g = -17.27$. This is shown in figure 20(*b*), representing a continuation of travelling-wave solutions at $Re = 15.72$, where we have varied Re_g. The solution curve exhibits a limit point at $Re_g \approx -10$ that precludes reaching the target value $Re_g = -17.27$.

We have also performed a transient computation on an open domain with inlet/outlet conditions, where we set $Re = 15.72$ and forced waves of frequency $f = f_{max}(Re_g = -17.27) = 0.73$, while gradually increasing Ψ from $\Psi = 1$ according to a sigmoid function. This computation produces occlusion long before Ψ has reached the target value $\Psi = 237$, which corresponds to the upper solution branch in figure 20(*a*). We may thus conclude that Re_{max}, which is based on the limit point in figure 13(*a*), remains a representative occlusion bound also in the counter-current configuration.

Appendix D. Effect of axial viscous diffusion in figure 4(*a*)

Figure 21 represents a version of the computation from figure 4(*a*) where we have deactivated axial viscous diffusion, by setting $J_j = K_j = L_j = M_j = 0$ in (2.5*b*).

https://doi.org/10.1017/jfm.2020.267 Published online by Cambridge University Press

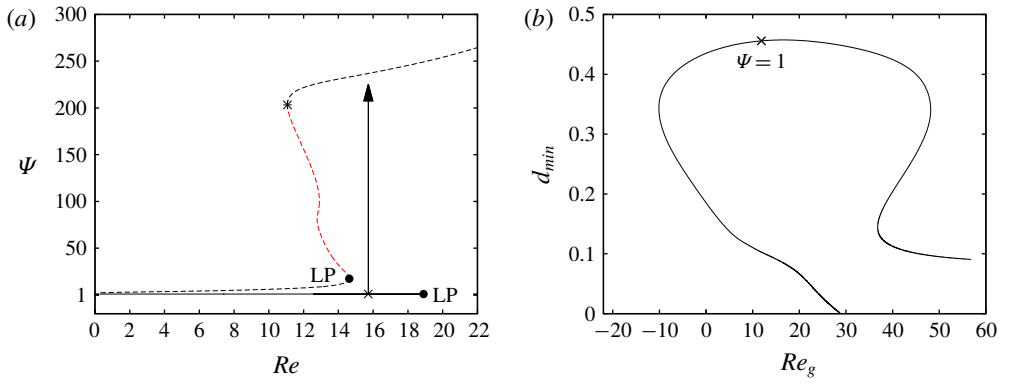


FIGURE 20. Travelling waves under the effect of a counter-current gas flow: case 4, $f = f_{max}$. (*a*) New representation of the curves from figure 13(*a*) in terms of the normalized pressure gradient $\Psi = \Delta p_g Fr^2$. Solid: aerostatic pressure drop, $\Psi = 1$. Dashed: counter-current gas flow, $Re_g = -17.27$. Solutions between the circle and asterisk (red segment) are stable. Filled circles correspond to limit points in figure 13(*a*). (*b*) Variation of the gas Reynolds number Re_g at $Re = 15.72$. The intended continuation path is indicated by an arrow in panel (*a*).

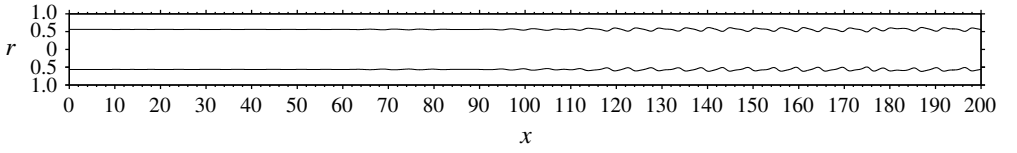


FIGURE 21. Version of the computation from figure 4(*a*) with axial viscous diffusion deactivated: $J_j = K_j = L_j = M_j = 0$ in (2.5). The film surface is represented at the same time as in figure 4(*a*).

In contrast to figure 4(*a*), no occlusion is observed over the entire length of the tube, which is in qualitative contradiction with the experiments of Camassa *et al.* (2014).

Appendix E. Improved representation of liquid plugs

Inspired by the use of an additional attractive–repulsive force term to model contact line problems within the framework of film models (Thiele *et al.* 2001), we add a repulsive azimuthal capillary term to the right-hand side of our model equation (2.5*b*):

$$\Pi_\theta = We^{-1} \exp\left[\lambda\left(1 - \frac{d(x,t)}{d_{plug}}\right)\right] \partial_x \kappa_\theta, \quad \kappa_\theta = -\frac{1}{d}\left[1 - \frac{1}{2}(\partial_x d)^2\right]. \tag{E 1}$$

As a result of its exponential variation with d (which can be scaled with λ), the effect of this term is significant only in the vicinity of the predefined radius d_{plug}, which is set to a small fraction of the tube radius R. At $d = d_{plug}$, Π_θ exactly compensates the capillary pressure gradient due to (destabilizing) azimuthal curvature. Furthermore, by adequately choosing d_{plug} and λ, the primary flow with a cylindrical film surface at $d = d_{plug}$ can be rendered linearly stable at all wave numbers (we have checked this with spatial linear stability analysis). This allows representing liquid plugs as stable travelling liquid annuli, or pseudo-plugs, that almost entirely fill the tube cross-section.

https://doi.org/10.1017/jfm.2020.267 Published online by Cambridge University Press

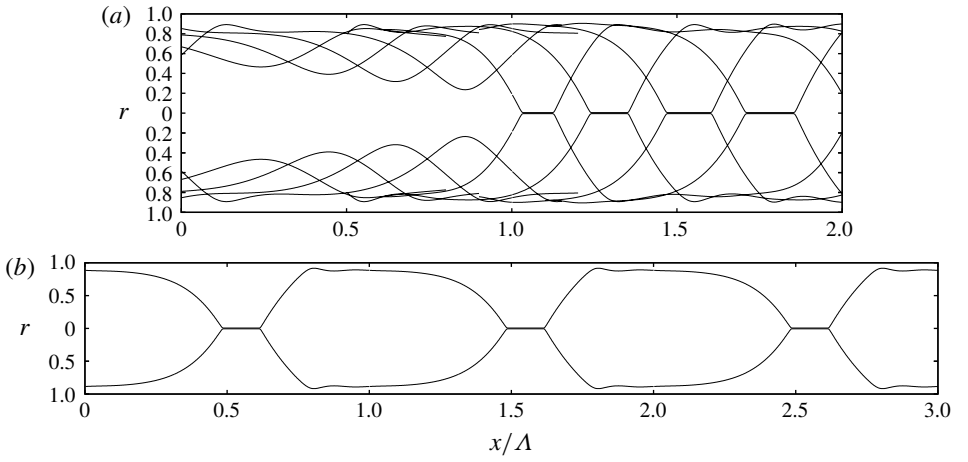


FIGURE 22. Improved representation of liquid plugs. Transient periodic computation based on the WRIBL model (2.5) upgraded with the localized repulsive term Π_θ (E 1), using $d_{plug} = 0.01R$ and $\lambda = 1$. Case 4: $\Lambda = 5.40$; $V_l/\pi/R^3 = 2.80$. (*a*) Surface profiles at times $t^\star/t_v^\star = 20,\ 30,\ 40,\ 50,\ 60,\ 70,\ 80,\ 90$ ($t_v^\star = \nu_l^{1/3} g^{-2/3} = 0.0037$ s) during the formation of a pseudo-plug. The four last profiles have been shifted by one wavelength to better guide the eye. (*b*) Fully developed pseudo-plugs: $t^\star/t_v^\star = 300$. The periodic surface profile has been reproduced three times here.

Figure 22 represents results of a transient periodic computation based on our WRIBL model (2.5) with the additional force term Π_θ (E 1). Liquid properties and tube radius correspond to case 4, which, due to the relevance of inertia, is the most challenging. Furthermore, $\Lambda = 5.40$, $V_l/\pi/R^3 = 2.80$, $d_{plug} = 0.01R$ and $\lambda = 1$. Figure 22(*a*) represents the time evolution of the film surface during formation of a pseudo-plug, and figure 22(*b*) represents the fully developed pseudo-plug. To better guide the eye, we have reproduced and shifted the periodic surface profile in these panels.

In contrast to the crude numerical core radius limitation employed in our open-domain computations, our improved representation of liquid plugs ensures volume conservation and, thus, the pseudo-plug in figure 22 does not reopen. On the downside, this new representation requires a finer spatial numerical resolution. Thus, open-domain computations, such as the one in figure 17(*a*), become more costly (about four times for case 4). This can be alleviated by implementing a locally refined grid in the plug regions, following the example of Lister *et al.* (2006) for the representation of locally thin liquid films. We leave this task, and the confrontation of our pseudo-plug model with full-fledged plug models for pressure driven core-annular flows (Ubal *et al.* 2008) or inclined planar channel flows (Suresh & Grotberg 2005), to future work. In the latter case, our additional force term (E 1) would have to be adapted to a planar geometry.

REFERENCES

ALBERT, C., MARSCHALL, H. & BOTHE, D. 2013 Direct numerical simulation of interfacial mass transfer into falling films. *Intl J. Heat Mass Transfer* **69**, 343–357.

ALEKSEENKO, S. V., AKTERSHEV, S. P., CHERDANTSEV, A. V., KHARLAMOV, S. M. & MARKOVICH, D. M. 2009 Primary instabilities of liquid film flow sheared by turbulent gas stream. *Intl J. Multiphase Flow* **35**, 617–627.

https://doi.org/10.1017/jfm.2020.267 Published online by Cambridge University Press

AUL, R. W. & OLBRICHT, W. L. 1990 Stability of a thin annular film in pressure-driven, low-Reynolds-number flow through a capillary. *J. Fluid Mech.* **215**, 585–599.

BELTRAME, P. 2018 Partial and complete wetting in a micro-tube. *Europhys. Lett.* **121**, 64002.

BENNEY, D. J. 1966 Long waves on liquid films. *J. Math. Phys.* **45**, 150–155.

BIAN, S., TAI, C.-F., HALPERN, D., ZHENG, Y. & GROTBERG, J. B. 2010 Experimental study of flow fields in an airway closure model. *J. Fluid Mech.* **647**, 391–402.

BRACKBILL, J. U., KOTHE, D. B. & ZEMACH, C. 1992 A continuum method for modelling surface tension. *J. Comput. Phys.* **100**, 335–354.

BROOKE BENJAMIN, T. 1957 Wave formation in laminar flow down an inclined plane. *J. Fluid Mech.* **2**, 554–574.

CAMASSA, R., FOREST, M. G., LEE, L., OGROSKY, H. R. & OLANDER, J. 2012 Ring waves as a mass transport mechanism in air-driven core-annular flows. *Phys. Rev.* E **86** (6), 066305.

CAMASSA, R., MARZUOLA, J. L, OGROSKY, H. R. & VAUGHN, N. 2016 Traveling waves for a model of gravity-driven film flows in cylindrical domains. *Physica* D **333**, 254–265.

CAMASSA, R., OGROSKY, H. R. & OLANDER, J. 2014 Viscous film-flow coating the interior of a vertical tube. Part 1. Gravity-driven flow. *J. Fluid Mech.* **745**, 682–715.

CAMASSA, R., OGROSKY, H. R. & OLANDER, J. 2017 Viscous film-flow coating the interior of a vertical tube. Part 2. Air-driven flow. *J. Fluid Mech.* **825**, 1056–1090.

CHANG, H. C., DEMEKHIN, E. A. & KALAIDIN, E. 1996*a* Simulation of noise-driven wave dynamics on a falling film. *AIChE J.* **42** (6), 1553–1568.

CHANG, H. C., DEMEKHIN, E. A., KALAIDIN, E. & YE, Y. 1996*b* Coarsening dynamics of falling-film solitary waves. *Phys. Rev.* E **54** (2), 1467–1477.

CHANG, H. C., DEMEKHIN, E. A. & KOPELEVICH, D. I. 1993 Nonlinear evolution of waves on a vertically falling film. *J. Fluid Mech.* **250**, 433–480.

DAO, E. K. & BALAKOTAIAH, V. 2000 Experimental study of wave occlusion on falling films in a vertical pipe. *AIChE J.* **46** (7), 1300–1306.

DELAUNAY, C. 1841 Sur la surface de révolution dont la courbure moyenne est constante. *J. Math. Pures Appl.* **6**, 309–320.

DIETZE, G. F. 2016 On the Kapitza instability and the generation of capillary waves. *J. Fluid Mech.* **789**, 368–401.

DIETZE, G. F. 2019 Effect of wall corrugations on scalar transfer to a wavy falling liquid film. *J. Fluid Mech.* **859**, 1098–1128.

DIETZE, G. F. & RUYER-QUIL, C. 2013 Wavy liquid films in interaction with a confined laminar gas flow. *J. Fluid Mech.* **722**, 348–393.

DIETZE, G. F. & RUYER-QUIL, C. 2015 Films in narrow tubes. *J. Fluid Mech.* **762**, 68–109.

DING, Z., LIU, Z., LIU, R. & YANG, C. 2019 Thermocapillary effect on the dynamics of liquid films coating the interior surface of a tube. *Intl J. Heat Mass Transfer* **138**, 524–533.

DOEDEL, E. J. 2008 *AUTO07p: Continuation and Bifurcation Software for Ordinary Differential Equations*. Montreal Concordia University.

DUPRAT, C., RUYER-QUIL, C., KALLIADASIS, S. & GIORGIUTTI-DAUPHINÉ, F. 2007 Absolute and convective instabilities of a viscous film flowing down a vertical fiber. *Phys. Rev. Lett.* **98**, 244502.

EVERETT, D. H. & HAYNES, J. M. 1972 Model studies of capillary condensation. *J. Colloid Interface Sci.* **38** (1), 125–137.

FRENKEL, A. L., BABCHIN, A. J., LEVICH, B. G., SHLANG, T. & SIVASHINSKY, G. I. 1987 Annular flows can keep unstable films from breakup: nonlinear saturation of capillary instability. *J. Colloid Interface Sci.* **115** (1), 225–233.

GAUGLITZ, P. A. & RADKE, C. J. 1988 An extended evolution equation for liquid film breakup in cylindrical capillaries. *Chem. Engng Sci.* **43** (7), 1457–1465.

GOREN, S. L. 1962 The instability of an annular thread of fluid. *J. Fluid Mech.* **12** (2), 309–319.

GROTBERG, J. 2011 Respiratory fluid mechanics. *Phys. Fluids* **23**, 021301.

HICKOX, C. E. 1971 Instability due to viscosity and density stratification in axisymmetric pipe flow. *Phys. Fluids* **14** (2), 251–262.

https://doi.org/10.1017/jfm.2020.267 Published online by Cambridge University Press

HIRT, C. W. & NICHOLS, B. D. 1981 Volume of fluid (VOF) method for the dynamics of free boundaries. *J. Comput. Phys.* **39**, 201–225.

JENSEN, O. E. 2000 Draining collars and lenses in liquid-lined vertical tubes. *J. Colloid Interface Sci.* **221**, 38–49.

JOSEPH, D. D., CHEN, K. P. & RENARDY, Y. Y. 1997 Core-annular flows. *Annu. Rev. Fluid Mech.* **29**, 65–90.

KALLIADASIS, S. & CHANG, H. C. 1994 Drop formation during coating of vertical fibres. *J. Fluid Mech.* **261**, 135–168.

KALLIADASIS, S., RUYER-QUIL, C., SCHEID, B. & VELARDE, M. G. 2012 *Falling Liquid Films*, Applied Mathematical Sciences, vol. 176. Springer.

KAMM, R. D. & SCHROTER, R. C. 1989 Is airway closure caused by a liquid film instability? *Respir. Physiol.* **75**, 141–156.

KAPITZA, P. L. 1948 Wave flow of thin layer of viscous fluid (in Russian). *Zh. Eksp. Teor. Fiz.* **18** (1), 3–28.

KING, M. & MACKLEM, P. T. 1977 Rheological properties of microliter quantities of normal mucus. *J. Appl. Phys.* **42** (6), 797–802.

KOURIS, C. & TSAMOPOULOS, J. 2001 Dynamics of axisymmetric core-annular flow in a straight tube. I. The more viscous fluid in the core, bamboo waves. *Phys. Fluids* **13** (4), 841–858.

LAVALLE, G., GRENIER, N., MERGUI, S. & DIETZE, G. F. 2020 Solitary waves on superconfined falling liquid films. *Phys. Rev. Fluids* **5**, 032001(R).

LEWIS, T. A., TZENG, Y.-S., MCKINSTRY, E. L., TOOKER, A. C., HONG, K., SUN, Y., MANSOUR, J., HANDLER, Z. & ALBERT, M. S. 2005 Quantification of airway diameters and 3D airway tree rendering from dynamic hyperpolarized 3He magnetic resonance imaging. *Magn. Reson. Med.* **53**, 474–478.

LISTER, J. R., RALLISON, J. M., KING, A. A., CUMMINGS, L. J. & JENSEN, O. E. 2006 Capillary drainage of an annular film: the dynamics of collars and lobes. *J. Fluid Mech.* **552**, 311–343.

LIU, J. & GOLLUB, J. P. 1993 Onset of spatially chaotic waves on flowing films. *Phys. Rev. Lett.* **70** (15), 2289–2292.

LIU, R. & DING, Z. 2017 Stability of viscous film flow coating the interior of a vertical tube with a porous wall. *Phys. Rev.* E **95** (5), 053101.

MATHEMATICA 2014 *Version 10.0.2.0*. Wolfram Research, Inc.

NOSOKO, T., YOSHIMURA, P. N., NAGATA, T. & OYAKAWA, K. 1996 Characteristics of two-dimensional waves on a falling liquid film. *Chem. Engng Sci.* **51** (5), 725–732.

PLATEAU, J. P. 1849 Recherches expérimentales et théoriques sur les figures d'équilibre d'une masse liquide sans pesanteur. *Mémoires de l'Académie Royale des Sciences, des Lettres et des Beaux-Arts de Belgique* **23**, 1–150.

POPINET, S. 2009 An accurate adaptive solver for surface-tension-driven interfacial flows. *J. Comput. Phys.* **228**, 5838–5866.

QUÉRÉ, D. 1990 Thin films flowing on vertical fibers. *Europhys. Lett.* **13** (8), 721–726.

QUÉRÉ, D. 1999 Fluid coating on a fibre. *Annu. Rev. Fluid Mech.* **31**, 347–384.

RAYLEIGH, LORD 1892 On the instability of cylindrical fluid surfaces. *Phil. Mag.* **34** (207), 177–180.

RICHARD, G., RUYER-QUIL, C. & VILA, J. P. 2016 A three-equation model for thin films down an inclined plane. *J. Fluid Mech.* **804**, 162–200.

SEEBAUER, F., POECHLAUER, P., BRAUNE, S. & STEINHOFER, S. 2012 Tube bundle falling film microreactor for performing gas liquid reactions. US Patent 8221708B2.

SHKADOV, V. Y. 1967 Wave flow regimes of a thin layer of viscous fluid subject to gravity. *Fluid Dyn.* **2** (1), 29–34.

SURESH, V. & GROTBERG, J. B. 2005 The effect of gravity on liquid plug propagation in a two-dimensional channel. *Phys. Fluids* **17** (3), 031507.

THIELE, U., VELARDE, M. G., NEUFFER, K & POMEAU, Y. 2001 Sliding drops in the diffuse interface model coupled to hydrodynamics. *Phys. Rev.* E **64** (6), 061601.

TRIFONOV, Y. Y. 1992 Steady-state traveling waves on the surface of a viscous liquid film falling down on vertical wires and tubes. *AIChE J.* **38** (6), 821–834.

https://doi.org/10.1017/jfm.2020.267 Published online by Cambridge University Press

TRIFONOV, Y. Y. 2010 Counter-current gas–liquid wavy film flow between the vertical plates analyzed using the Navier–Stokes equations. *AIChE J.* **56** (8), 1975–1987.

TSELUIKO, D. & KALLIADASIS, S. 2011 Nonlinear waves in counter-current gas–liquid film flow. *J. Fluid Mech.* **673**, 19–59.

UBAL, S., CAMPANA, D. M., GIAVEDONI, M. D. & SAITA, F. A. 2008 Stability of the steady-state displacement of a liquid plug driven by a constant pressure difference along a prewetted capillary tube. *Ind. Engng Chem. Res.* **47**, 6307–6315.

VLACHOS, N. A., PARAS, S. V., MOUZA, A. A. & KARABELAS, A. J. 2001 Visual observations of flooding in narrow rectangular channels. *Intl J. Multiphase Flow* **27**, 1415–1430.

WRAY, A. W. 2013 Electrostatically controlled large-amplitude, non-axisymmetric waves in thin film flows down a cylinder. *J. Fluid Mech.* **736**, R2.

XU, F. & JENSEN, O. 2017 Trapping and displacement of liquid collars and plugs in rough-walled tubes. *Phys. Rev. Fluids* **2**, 094004.

YIH, C. S. 1963 Stability of liquid flow down an inclined plane. *Phys. Fluids* **6** (3), 321–334.

YOSHIMURA, P. N., NOSOKO, P. & NAGATA, T. 1996 Enhancement of mass transfer into a falling laminar liquid film by two-dimensional surface waves—some experimental observations and modeling. *Chem. Engng Sci.* **51** (8), 1231–1240.

ZAPKE, A. & KRÖGER, D. G. 2000 Countercurrent gas–liquid flow in inclined and vertical ducts – I: flow patterns, pressure drop characteristics and flooding. *Intl J. Multiphase Flow* **26**, 1439–1455.

ZHOU, Z.-Q., PENG, J., ZHANG, Y.-J. & ZHUGE, W.-L. 2016 Viscoelastic liquid film flowing down a flexible tube. *J. Fluid Mech.* **802**, 583–610.

https://doi.org/10.1017/jfm.2020.267 Published online by Cambridge University Press